EarthArXiv Cover Sheet

Title

Timescale-dependent response of vegetation to climate change

Authors

David Fastovich[1], Stephen R. Meyers[2], Erin E. Saupe[3], John W. Williams[4], Maria Dornelas[5,6], Elizabeth M. Dowding[10], Seth Finnegan[8], Huai-Hsuan M. Huang[9], Lukas Jonkers[10], Wolfgang Kiessling[7], Ádám T. Kocsis[7], Qijian Li[11], Lee Hsiang Liow[12], Lin Na[11], Amelia M. Penny[13], Kate Pippenger[14], Johan Renaudie[15], Marina C. Rillo[16], Jansen Smith[17], Manuel J. Steinbauer[18], Mauro Sugawara[19,20], Adam Tomašovỳch[21], Moriaki Yasuhara[22,23], Pincelli M. Hull[14,24,25]

Affiliations

[1]Department of Earth and Environmental Sciences, Syracuse University, Syracuse, NY, USA
[2]Department of Geoscience, University of Wisconsin – Madison, Madison, WI 53706, USA
[3]Department of Earth Sciences, University of Oxford, South Parks Road, Oxford, OX1 3AN, United Kingdom
[4]Department of Geography & Center for Climatic Research, University of Wisconsin-Madison, 550 N. Park Street, Madison, WI 53706 USA
[5]Department of Earth and Planetary Sciences, Yale University, 210 Whitney Ave, New Haven, CT 06511, USA
[5]University of St Andrews, St. Andrews, United Kingdom
[6]Guia Marine Lab, MARE, Faculty of Science of the University of Lisbon, 939, Estrada do Guincho, Cascais 2750-374, Portugal
[7]GeoZentrum Nordbayern, Friedrich-Alexander Universität Erlangen-Nürnberg (FAU), Erlangen, Germany
[8]Department of Integrative Biology & Museum of Paleontology, University of California, Berkeley, Berkeley, CA USA
[9]Department of Geosciences, Princeton University, NJ, USA
[10]MARUM – Center for Marine Environmental Sciences University of Bremen, Bremen, Germany
[11]State Key Laboratory of Palaeobiology and Stratigraphy, Nanjing Institute of Geology and Palaeontology and Center for Excellence in Life and Paleoenvironment, Chinese Academy of Sciences, Nanjing, China
[12]Natural History Museum & Centre for Planetary Habitability, Department of Geosciences, University of Oslo, Oslo, Norway
[13]School of GeoSciences, University of Edinburgh, Edinburgh, United Kingdom
[14]Department of Earth and Planetary Sciences, Yale University, New Haven, CT, USA
[15]Museum für Naturkunde, Invalidenstraße 43, Berlin, Germany
[16]ICBM - Institute for Chemistry and Biology of the Marine Environment, University of Oldenburg, Wilhelmshaven, Germany
[17]Department of Earth & Environmental Sciences, University of Minnesota - Duluth, Duluth, MN, USA

[18]Bayreuth Center of Ecology and Environmental Research, University of Bayreuth, Bayreuth, Germany
[19]University of British Columbia, Vancouver, BC, Canada
[20]Mário Schenberg Institute, São Paulo, Brazil
[21]Earth Science Institute, Slovak Academy of Sciences, Bratislava, Slovakia
[22]School of Biological Sciences, Area of Ecology and Biodiversity, Swire Institute of Marine Science, Institute for Climate and Carbon Neutrality, Musketeers Foundation Institute of Data Science, The University of Hong Kong, Hong Kong, China
[23]State Key Laboratory of Marine Pollution, City University of Hong Kong, Hong Kong, China
[24]Yale Peabody Museum, 170 Whitney Ave, New Haven, CT, 06511, USA
[25]Swiss Federal Institute for Forest, Snow and Landscape Research, Birmensdorf, Switzerland

Corresponding Author

David Fastovich, dfastovi@syr.edu

Peer-review Statement

This manuscript has been submitted to *Science* and is not peer-reviewed. This preprint has been submitted to EarthArXiv. Subsequent versions of this manuscript may have slightly different content. If accepted, the final version of this manuscript will be available via the 'Peer-reviewed Publication DOI' link on the right-hand side of this webpage.

Abstract

Climate and ecosystems are dynamic across timescales, but existing research into climate-driven vegetation dynamics usually focuses on singular timescales. We develop a novel spectral analysis-based approach that provides unprecedentedly detailed estimates of the timescales at which vegetation tracks climate change, from 10^1 to 10^5 years. We report dynamic similarity of vegetation and climate at centennial frequencies (146^{-1} to $17{,}505^{-1}$ years^{-1}). A breakpoint in vegetation turnover (759^{-1} years^{-1}) matches a breakpoint between stochastic and autocorrelated climate processes, suggesting ecological dynamics are governed by climate across these regimes. However, heightened vegetation turnover at millennial frequencies ($4{,}650^{-1}$ years^{-1}) highlights the risk of abrupt ecological responses to climate change, while vegetation-climate decoupling at frequencies shorter than 146^{-1} years^{-1} suggests that plant assemblages may continue changing for centuries in response to anthropogenic climate change, with potentially lasting consequences for ecosystem function and biodiversity.

Keywords

Spectral power continuum, community turnover, climate variability, dynamic equilibrium, non-linear ecological dynamics, temporal beta diversity, vegetation

Manuscript Text

The biosphere is a dynamic component of the Earth system that is sensitive to climate variability, with eco-evolutionary processes operating across a broad range of timescales (*1–3*). Ecologists have long recognized that species and ecological systems differ in their responses to changing climate and that these dynamics are timescale dependent (*3–6*). However, most studies of climate-driven ecological dynamics have focused on recent baselines and narrow ranges of timescales, leaving critical gaps in our understanding of how communities respond to environmental change across the continuous range of timescales experienced by biota (*7*, *8*).

Recent advances have improved our understanding of climate variability (*9*, *10*) and expanded global networks of ecological and paleontological data across timescales (*11*, *12*). These parallel advances now enable us to characterize, in ways not previously possible, ecological responses to climate forcing as fast, slow, and/or nonlinear (*13*, *14*). Fast ecological dynamics can track climate change (*13*, *14*), while slow dynamics are lagged or decoupled from climate (*15–18*). Regardless of whether dynamics are fast or slow, ecosystems can linearly or nonlinearly respond to forcing (e.g. (*19*)), with the potential for nonlinear responses to lead to abrupt species compositional changes or other ecological regime shifts (*20*). Characterizing the nature of ecological dynamics across timescales is urgently required for understanding how and at what rates ecological systems are likely to respond to anthropogenic climate change (*21*).

Here, we focus on the relationship among temperature, precipitation, and vegetation compositional turnover in time series spanning hundreds to hundreds of thousands of years for the last 600,000 years, with the densest coverage for the last 20,000 years. To study the relationship between timescales of climate variability and vegetation dynamics, we create and apply a conceptual and analytical framework rooted in spectral analysis (*22*), widely used in

climate science (*9*, *23–25*). Spectral analysis decomposes the variance in a time series into its constituent frequencies, providing insights into the relative contributions of different timescales to the overall variability. Within this framework, vegetation variability is characterized by change (or turnover) in species composition within assemblages as measured with the squared chord dissimilarity metric (*26*). Comparing climate and vegetation variability in the frequency domain overcomes a fundamental challenge in time-domain analyses: the coupling, decoupling, and scaling of climate drivers and ecological responses with time.

Through this approach, we generate global power spectra of vegetation variability by averaging site-level power spectra for fossil pollen assemblages across a global compilation of 1,321 sites. We compare these global vegetation compositional changes to power spectra of temperature and precipitation from a climate model simulation of the last 21,000 years (TraCE-21ka) (*27*, *28*). To capture lower-frequency climate variability than that covered by the 21,000 year-long simulation, we include climate reconstructions that approximate global climate from an Antarctic ice core (*29*) and a proxy-based reconstruction of global surface air temperature of the last two million years (*30*). By comparing the global dynamics of climate and vegetation across timescales, we assess the coupling of vegetation assemblages to climate variability.

Paired Spectral Analysis of Climate and Vegetation: Analytical and Conceptual Framework

Paired spectral analyses of climate and ecological time series can quantify the dynamic similarity of climate and assemblage turnover across timescales (*31*, *32*). In frequency space, timescale and frequency are inversely related – longer timescales correspond to lower frequencies and short timescales correspond to higher frequencies. The dynamics of climate and vegetation can be assessed in frequency space by comparing their spectral continua. For many physical systems, the exponential coefficient of the power-law relationship (β in $S(f) \propto f^{-\beta}$) between spectral power (S) and frequency (f) defines the spectral continuum. Within a time series, β characterizes memory (i.e. temporal autocorrelation) and how variance is partitioned across frequencies (*25*). If the exponential coefficient (β) of the power-law relationship between frequency and spectral power is small ($\beta \sim 0$), variance is equally partitioned among all frequencies (i.e., white noise; Figure S1) (*25*). In contrast, $\beta > 0$ indicates more variance at lower frequencies (longer periods), with $\beta = 2$ defining a random walk (i.e., red noise; Figure S1) (*25*).

There exists a scale break in the spectral continuum of climate variability between short-lived, stochastic, weather processes and climate processes that possess increasing variability with decreasing frequency (*33*). This break occurs between 100^{-1} to $1{,}000^{-1}$ $years^{-1}$ and separates high frequencies that are represented by a low β from low frequencies that are characterized by a high β (*9*, *10*). If vegetation composition changes in parallel with climate variability, then variability in vegetation turnover should have similar βs and show a similar scaling break (Figure 1A, $\beta_{veg} = \beta_{clim}$). However, the drivers of vegetation compositional change vary in relative importance across frequencies (Figure 1): disturbance, biotic interactions, and demographic processes are thought to be more important at high frequencies; dispersal limitation, population dynamics, restriction to refugia, and ecosystem transformation dominate at intermediate frequencies; and macroevolutionary processes such as speciation and extinction prevail at lower frequencies

(Figure 1)(*1*, *2*). These processes may modulate vegetation responses to climate and may cause the continuum of vegetation variability to diverge from climate.

We expect that matching βs for climate and climate and vegetation (i.e. $\beta_{veg} = \beta_{clim}$) are likely to emerge at intermediate frequencies (i.e. millennial to orbital cycles, roughly $1{,}000^{-1}$ to $100{,}000^{-1}$ years^{-1}) (*13*, *14*), where plant assemblages are influenced by ecological and biogeographic processes such as environmental filtering, dispersal, restriction to refugia, and local population extirpation (*34*, *35*) (Figure 1). At these intermediate frequencies, the processes determining assemblage composition, such as dispersal and ecosystem transformations caused by changing species' abundances, act quickly relative to the pacing of climate variability (*13*, *14*). Here, we use the term 'fast tracking' to refer to cases where vegetation and climate have matching βs, even though our methods do not test for causation. Built upon this expectation of fast tracking at these frequencies, many prior studies have used pollen and other microfossils as paleoclimate proxies (*36*–*39*).

However, the relationship between climate and vegetation dynamics at lower ($< 100{,}000^{-1}$ years^{-1}) and higher frequencies ($> 1{,}000^{-1}$ years^{-1}) remains an open question, as does the exact frequencies at which the assumption of fast tracking no longer holds (*15*). High frequencies are particularly crucial for predicting vegetation responses to anthropogenic climate warming, as they allow exploration of how ecological and life-history factors may override the influence of climate variability. The vegetation response at high frequencies may be slow because trees tend to have lifespans of 10^1 to 10^3 years (*40*). This characteristic may produce low variability in vegetation turnover at high frequencies, but high variability at frequencies corresponding with tree senescence—manifesting as a larger β in vegetation turnover than in climate (Figure 1B, $\beta_{veg} > \beta_{clim}$). Conversely, disturbance through herbivory, fire, human land use, and disease could increase vegetation turnover at high frequencies, thereby causing a smaller β relative to climate (Figure 1B, $\beta_{veg} < \beta_{clim}$).

At low frequencies, vegetation dynamics distinct from intermediate and short frequencies may emerge. Climate tracking could persist, as expected at intermediate frequencies (Figure 1C, $\beta_{veg} = \beta_{clim}$), or adaptive evolution could increase species' tolerances to new climate regimes (*41*), potentially reducing assemblage compositional responses to climate forcing and species' sensitivity to environmental changes. As a product of compositional stability, vegetation turnover variability would increase minimally as frequencies decrease relative to climate variations. (Figure 1C, $\beta_{veg} < \beta_{clim}$). Conversely, if vegetation responses to environmental forcings are characterized by strong non-linearities (*42*–*44*), variability in vegetation turnover would be high relative to climate and vegetation turnover variability would increase as frequency decreases faster than climate variability (Figure 1C, $\beta_{veg} > \beta_{clim}$) (*45*).

Spectral continuum of vegetation variability

To minimize sampling effects when comparing the power spectrum of vegetation variability to that of climate variability, we downsample and low-pass filter the simulated climate time series from TraCE-21ka to match the spatiotemporal characteristics of the fossil pollen archives (see Supplemental Information). Unlike simulated data, climate proxy data cannot undergo this processing, resulting in spatiotemporal characteristics that differ from the fossil pollen records.

We assess the effects of temporal uncertainty and uneven spatiotemporal coverage of the vegetation turnover data on the global power spectra (Figure 2) by resampling sites and their corresponding posterior age estimates to produce an ensemble of power spectra, estimates of β, and estimates of the breakpoints in β (see Methods).

We find that the spectral continuum of variability in vegetation turnover carries clear similarities to that of the climate system (Figure 2), yet the relationship to climate variability varies with frequency. The power spectrum of vegetation turnover appears to follow the climate system across the weather-climate breakpoint reported in previous studies (*9*, *10*, *23*, *46*) and found here (Figure 2, Table S1, 668^{-1}—647^{-1} $years^{-1}$ for temperature; 691^{-1}—661^{-1} $years^{-1}$ for precipitation; 802^{-1}—768^{-1} $years^{-1}$ for vegetation turnover), supporting the interpretation that vegetation dynamically tracks the climate system at intermediate frequencies (Figure 1, Figure 2) (*13*). However, unlike temperature and precipitation in our analyses (Figure 2) or in previous studies (*9*, *10*, *23*, *46*), the vegetation turnover power spectrum has two additional breakpoints, determined using segmented regressions (*47*), at 146^{-1} $years^{-1}$ (95% CI: 150^{-1}, 141^{-1}) and $17{,}505^{-1}$ $years^{-1}$ ($18{,}162^{-1}$, $16{,}831^{-1}$) (uncertainties for all parameters estimated are reported in Table S1). The vegetation turnover power spectra are therefore characterized by four scaling regimes: high frequencies (< 146^{-1} $years^{-1}$); high-intermediate frequencies (146^{-1} to 759^{-1} $years^{-1}$); low-intermediate frequencies (759^{-1} to $17{,}505^{-1}$ $years^{-1}$); and low frequencies (> $17{,}505^{-1}$ $years^{-1}$). The additional breakpoints in β in the vegetation turnover power spectrum found in the full ensemble (Figure 1) are also found in the spectra of well-resolved individual time series (Figure S2), indicating the patterns are not an artifact of the ensemble approach. Together, these features of the vegetation turnover power spectra provide striking evidence that the relationship between plant communities and climate is timescale-dependent and complex. Ecological communities and climate may co-vary on some timescales but differ in their dynamics on others, which we detail below.

Timescales of Ecological Dynamics

We find evidence of climate and vegetation coupling between the frequencies of 146^{-1} to $17{,}505^{-1}$ $years^{-1}$ (Figure 2), where the continuum of vegetation turnover and climate variability have similar βs. Specifically, βs are near zero at frequencies from 146^{-1} to 759^{-1} $years^{-1}$, and ~2 at frequencies from 759^{-1} to $17{,}505^{-1}$ $years^{-1}$. Moreover, the alignment of climate and vegetation turnover breakpoints between 664^{-1} and 759^{-1} $years^{-1}$ provides strong evidence of vegetation and climate coupling even across the transition from weather to climate regimes. Although the breakpoint for vegetation turnover is statistically distinguishable from that of temperature and precipitation (Table S5), these small differences may reflect the limitations of the approach rather than actual differences in timing. The non-random subset of communities recorded by these vegetation assemblage records, our choice of climate model, or biased local/regional spectral estimates from climate models (*46*, *48*) all could affect the precise location of the breakpoint and lead to an apparent offset. However, if this offset between the vegetation and climate breakpoints is real rather than an artifact, two hypotheses may explain the brief decoupling of climate and vegetation between frequencies of 675^{-1}—664^{-1} $years^{-1}$ and 759^{-1} $years^{-1}$: a lag in vegetation response to the transition from low, β weather to higher β, climate regimes or the greater importance of non-climatic forcing (such as disturbance regimes) at these frequencies.

This finding sharpens our understanding of the frequencies at which plant communities rapidly and dynamically adjust composition and structure in response to climate forcing (*49*). Prior theory and the observations of orbital signals in pollen records have led to the widespread agreement of fast tracking of climate by vegetation composition at frequencies of $1{,}000^{-1}$ to $100{,}000^{-1}$ years^{-1} (*13*, *14*). Vegetation turnover from climate warming during the last deglaciation illustrates this phenomenon particularly well (*50*). During this time interval, the climate system was characterized by millennial- to orbital-scale climate variability in temperature and precipitation (*51*, *52*), which have been identified as the primary correlates of vegetation turnover across these frequencies (*49*, *50*, *53–55*). However, whether vegetation rapidly tracks climate at sub-millennial frequencies (10^{-2} to 10^{-3} years^{-1}) is unclear (*14*), and there is evidence for and against climate disequilibrium at frequencies of 50^{-1} to 200^{-1} years^{-1} (*15*, *49*). Our work thus expands prior knowledge by suggesting climate tracking by vegetation for frequencies as short as 146^{-1} years^{-1}.

Unlike frequencies between 146^{-1} and $17{,}505^{-1}$ years^{-1}, the highest and lowest frequency bands exhibit climate decoupling. β is 4.58 (4.02, 5.12) for vegetation turnover at the highest frequencies, while for temperature and precipitation, β is -0.28 (-0.33, -0.21) and -0.52 (-0.59, -0.47), respectively (Figure 2, Table S1). This finding supports prior observations of higher βs in vegetation turnover at these high frequencies (*56*) but appears sensitive to the amount of weight given to abundant and rare taxa in the dissimilarity metric and the fossil pollen record under consideration (Figure S3). Some combination of taphonomy, sampling, and ecological processes could explain higher βs in vegetation turnover at these high frequencies. Decadal-scale mixing of lake sediments (*57*), scale gaps caused by discontinuous sampling of sediments (*12*), and variable record length may enhance autocorrelation in vegetation variability from these archives (*58*). In addition, the large βs at the highest frequencies may be due to the long life spans of some plants (e.g. trees, which are well-represented in fossil pollen assemblages), limiting the ability of the full assemblage to track high frequency climate due to slow turnover times (*56*). Indeed, the median tree lifespan from the International Tree Ring Data Bank (*59*, *60*) is 246 years (n = 4,773) (Figure S4), which may impart a high β as vegetation turnover would increase approaching the frequency of median tree longevity from increasing senescence. Furthermore, anthropogenic land use change may contribute to climate decoupling at high frequencies (*61*, *62*), possibly interacting with tree longevity. Finally, a greater β for vegetation turnover at the highest frequencies is consistent with observations of slow vegetation responses to climate variability and evidence of climate debt (*16–18*, *63*). These slow responses are expected to create mismatches between species' climate preferences and ambient climates and thus reduce organismal fitness and ecosystem function.

In the low-frequency band (frequencies lower than $17{,}505^{-1}$ years^{-1}, 95% CI: $18{,}162^{-1}$, $16{,}831^{-1}$), we observe β=-0.28 (-0.47, -0.10) for vegetation turnover power spectra (Figure 2). A low β for vegetation turnover in the low frequency band contrasts with the climate power spectra, which maintain the long-term climate system βs of ~2-3 due to the influence of astronomical forcing of ice sheets (Figure 2) (*64*, *65*). There are two possible explanations for low βs in vegetation turnover at these low frequencies. First, a low vegetation turnover β may reflect the saturation of community dissimilarity metrics used to compare vegetation assemblages across the time series, (Figure S5) which fail to record turnover beyond a complete replacement of the vegetation

assemblage (*66*). If climate change is large enough to have produced multiple assemblage turnovers (species assemblage A replaced by B replaced by C), community dissimilarity metrics will underestimate the true ecological impact of past climate change producing an apparent decrease in vegetation turnover with decreasing frequency. The second potential explanation for the low β at frequencies below $17{,}505^{-1}$ $years^{-1}$ is fast evolutionary adaptation by species to environmental variation that results in vegetation communities appearing relatively resistant to climate forcing. Although local adaptation cannot be excluded, the hypothesis of metric saturation appears sufficient to explain the reduced vegetation turnover variability at low frequencies (Figure S3).

Non-Linearity in the Climate-Vegetation Relationship

High spectral power at $4{,}650^{-1}$ $years^{-1}$ is unique to vegetation turnover and is absent in the power spectra of climate proxies and climate simulations (Figure 2, Figure S13) (*9*, *10*). Climate in the North Atlantic has been argued to contain apparent modes of climate variability at $1{,}470^{-1}$ and $4{,}670^{-1}$ $years^{-1}$ (*67*) and provide a plausible mechanism for forcing vegetation turnover (*37*, *49*, *68*). However, global compilations of Holocene climate records lack high spectral power at any of these frequencies (*69*), as do our power spectra of temperature and precipitation (Figure 2). This disconnect at the global scale (and in the subset of sites we investigated) between climate and vegetation turnover leads us to hypothesize that relatively subtle or regional millennial-scale climate variations are amplified in the vegetation signal by non-linear ecological dynamics (*42*, *70*).

However, analytical artifacts could contribute to high spectral power at $4{,}650^{-1}$ $years^{-1}$. Most of our records span the last 20,000 years with fewer long records exceeding that duration (186 sites, Figure S6, Table S2). The relatively low number of sites sampled could bias our spatial and environmental coverage at low frequencies, producing a spurious peak in spectral power. Despite these potential artifacts, evidence for nonlinear responses in vegetation assemblages to small environmental changes is well-documented (*42*). Our observations suggest slow vegetation responses to climate variability at high frequencies alongside high turnover at $4{,}650^{-1}$ $years^{-1}$, demonstrating how gradual vegetation changes can lead to abrupt, nonlinear shifts in vegetation assemblages. Hence, even without clear patterns of climate variability in the North Atlantic at this frequency, the vegetation dynamics over the last 600,000 years underscore the potential for abrupt changes in plant communities over the coming decades of warming (*71*, *72*).

Latitudinal Gradient in Assemblage Dynamics

We find that the relationship between vegetation turnover variability and climate variability differs across latitudes. Climatically, the high latitudes experience greater temperature variability than the tropics at all frequencies, while the tropics experience greater precipitation variability (Figure 3) (*9*). Vegetation turnover appears to resemble temperature, in that tropical sites (< 23.5°) have less vegetation variability than extra-tropical sites (> 23.5°), although the power spectra have overlapping confidence bounds across most of frequency space (Figure 3A). This overlap is caused mostly by larger differences among tropical vegetation turnover power spectra. At frequencies of 696^{-1} (722^{-1}, 680^{-1}) to $14{,}289^{-1}$ ($15{,}017^{-1}$, $13{,}797^{-1}$) $years^{-1}$, extra-tropical sites have a β of 2.21 (2.17, 2.26) that is similar to those of temperature and precipitation, while

tropical sites appear to have a β of 1.20 (1.14, 1.29) (Figure 3). Thus, there is the possibility that tropical vegetation assemblages are less sensitive to climate forcing across the frequencies investigated, are sensitive to climate forcings other than temperature and precipitation, are affected more by non-climatic factors, or are more stable and resistant to turnover. Along these lines, recent observations show that while net primary production in low latitudes is constrained by solar radiation and precipitation, high northern latitude productivity is limited by temperature (*73*), suggesting these latitudinal differences in β could result from spatially variable climate controls on vegetation variability.

Conclusions

Our novel and adaptable theoretical framework based on spectral analyses provides a new pathway forward to disentangle a fundamental question in ecology: how closely are ecological dynamics coupled or decoupled with environmental drivers across timescales? The methods shown here are flexible and adaptable to all ecological systems with observational data across a range of timescales.

Through this framework, we show that the relationship between vegetation turnover and climate variability is non-linear and timescale-dependent over frequencies from 10^{-1} to $100{,}000^{-1}$ years^{-1}. We show evidence for vegetation tracking climate change at frequencies of 146^{-1}- $17{,}505^{-1}$ years^{-1}, which is a narrower range of frequencies than previously theorized (*13*). This time period of fast vegetation tracking spans across the theorized (*33*) and observed scaling break (*9*, *10*) that separates weather and climate variability, which in turn suggests that a foundational shift of ecological variability from more red-noise to more white-noise at frequencies of ca. 700^{-1} years^{-1} is directly governed by coupled atmosphere-ocean processes. Modes of heightened variability in vegetation relative to climate at millennial frequencies underscore the risk of nonlinear and abrupt vegetation responses to current climate change. Conversely, the decoupling of vegetation and climate variability at higher frequencies (higher than 146^{-1} years^{-1}) is consistent with, and reinforces, concerns that biotic processes will be slow to respond to contemporary climate warming and changing climate variability (*15*). Consequently, the fast rate of anthropogenic climate change likely will outstrip the response time of plant communities in the next century, leading to delayed and widespread ecological transitions that challenge predicting vegetation responses to current warming.

Acknowledgments

This project is a contribution to the BioDeepTime project, supported by Paleosynthesis Project, which is funded by the Volkswagen Foundation (Az 96 796). DF acknowledges postdoctoral support from NSF OCE-2103015, NSF AGS-2402498, and the College of Arts and Sciences at Syracuse University. We are grateful to Yasuhiro Kubota for convening the P-SEEDS workshop where the idea for this project began. Many thanks to the Syracuse University High Throughput Computing Campus Grid (OrangeGrid) for providing computational resources and to Jon Cheney for technical support. Funding for OrangeGrid is provided by ACI-1341006. EES acknowledges support from a Leverhulme Prize and NERC grant NE/V011405/1. L.J. is supported through the German climate modeling initiative PALMOD, funded by the German Ministry of Science and Education (BMBF, 01LP1922A). PMH acknowledges sabbatical

support from the Swiss Federal Institute for Forest, Snow and Landscape Research. SRM acknowledges sabbatical support from UW-Madison and a Guggenheim Fellowship. JWW acknowledges sabbatical support from UW-Madison and NSF award 2410961. Fossil pollen data were obtained from the Neotoma Paleoecology Database (http://www.neotomadb.org) and its constituent databases: the African Pollen Database, European Pollen Database, Indo-Pacific Pollen Database, Latin American Pollen Database, and North American Pollen Database. The work of data contributors, data stewards, and the Neotoma community is gratefully acknowledged. We thank the anonymous reviewers for their feedback, which greatly improved the manuscript.

Data Availability Statement

Data and code needed to reproduce all analyses are available on Zenodo (*74*).

Author Contributions

DF and PMH developed the research questions and study design. DF, SRM, EES, JWW, and PMH co-developed the theoretical framework. DF performed all analyses with help from SRM and EES. DF led writing with support from SRM, EES, JWW, and PMH. The ideas for this paper originated from discussions in the BioDeepTime working group. All authors reviewed and contributed to the article.

Figures

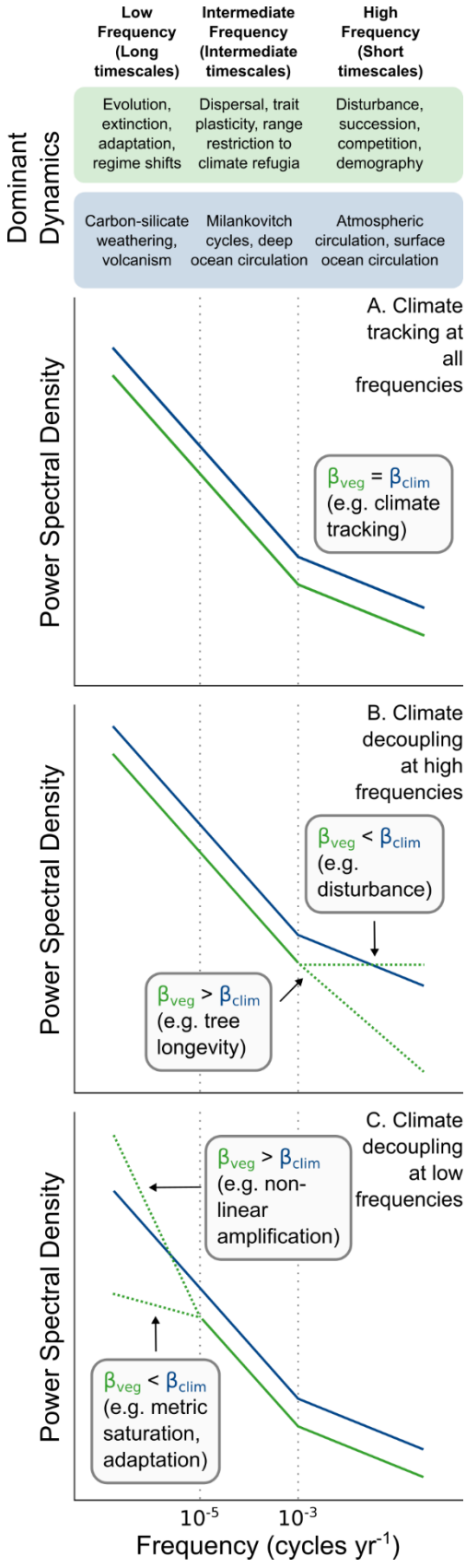
Low Frequency (Long timescales)
Intermediate Frequency (Intermediate timescales)
High Frequency (Short timescales)
Dominant Dynamics
Evolution, extinction, adaptation, regime shifts
Dispersal, trait plasticity, range restriction to climate refugia
Disturbance, succession, competition, demography
Carbon-silicate weathering, volcanism
Milankovitch cycles, deep ocean circulation
Atmospheric circulation, surface ocean circulation
A. Climate tracking at all frequencies
Power Spectral Density
βveg = βclim (e.g. climate tracking)
B. Climate decoupling at high frequencies
βveg < βclim (e.g. disturbance)
βveg > βclim (e.g. tree longevity)
C. Climate decoupling at low frequencies
βveg > βclim (e.g. non-linear amplification)
βveg < βclim (e.g. metric saturation, adaptation)
10-5
10-3
Frequency (cycles yr-1)

Figure 1. A conceptual framework for interpreting the relationship between vegetation and climate using power spectra through the power-law scaling relationship between spectral power and frequency ($S(f) \propto f^{-\beta}$). The blue line corresponds to β for climate variability and the green line corresponds to β for vegetation compositional turnover. The breakpoint in climate spectral power in all three panels is based on prior work that indicates a breakpoint in climate variability at approximately 100^{-1} to $1{,}000^{-1}$ $years^{-1}$ (*9*, *10*). Key phenomena include the slope (β, i.e. continuum) of vegetation turnover relative to climate and the placement of breakpoints (dashed vertical lines). Three scenarios illustrate potential relationships between climate and vegetation. (A) Vegetation composition exhibits linear responses to climate across all frequencies and so the slope of vegetation spectral power parallels that of climate (*13*). (C) Vegetation tracks climate across high and intermediate frequencies but is decoupled at low frequencies from processes like evolutionary adaptation (lower β for vegetation) or non-linear amplification through processes such as threshold responses (higher β for vegetation). Other scenarios and ecological processes are possible beyond those shown here.

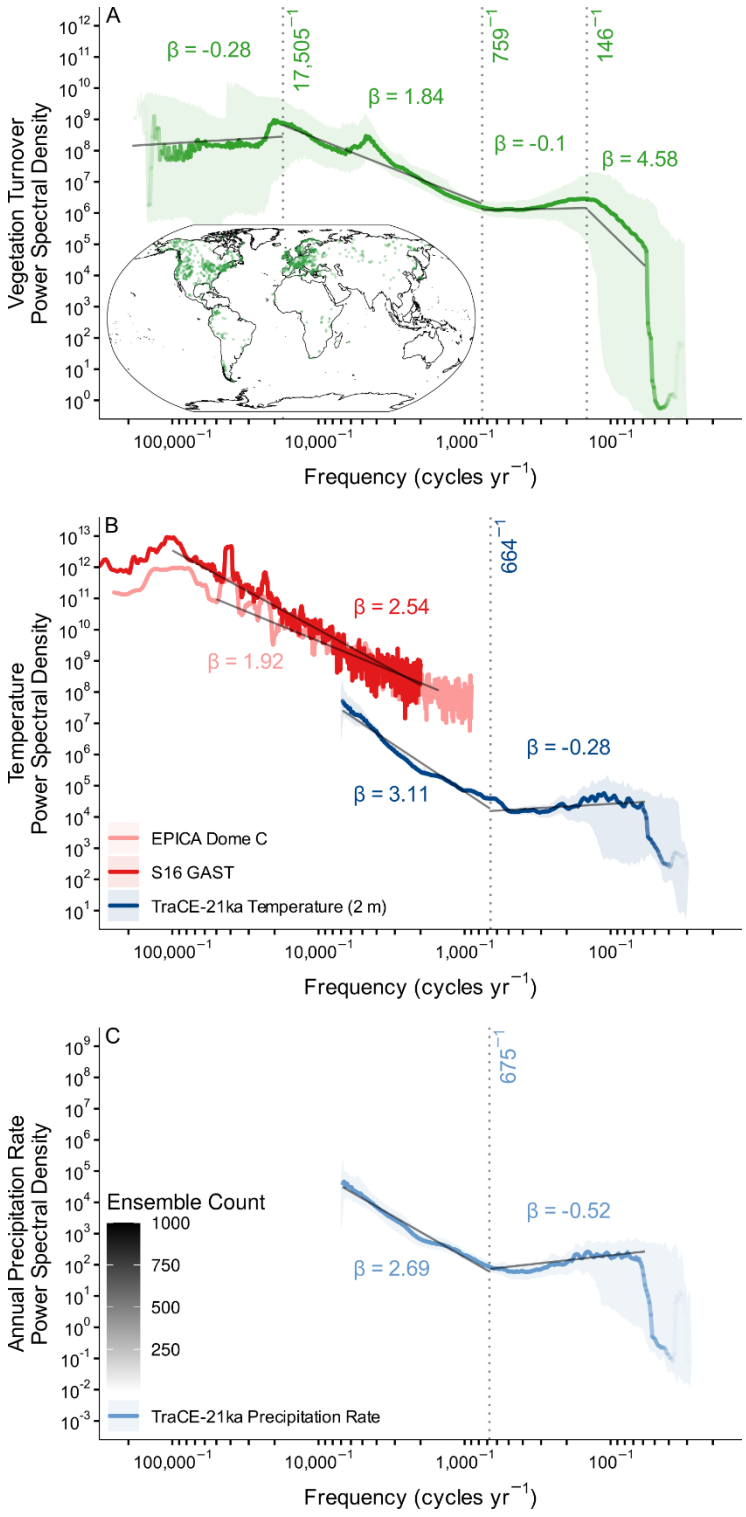

Figure 2. The spectral continuum of (A) vegetation turnover (green), (B) temperature (blue, red, pink), and (C) precipitation (light blue) variability based on the median from an ensemble of spectral power estimates. Power spectra line opacity indicates the number of ensemble members that resolve each frequency with the corresponding legend for all plots in (C). β in the high frequency band was fit to the maximum frequency that yielded an unbiased estimate (Supplementary Information). Solid gray lines correspond to β from ordinary least squares

regressions of log-spectral power and log-frequency. Vertical dashed lines correspond to breakpoints identified in the spectral continuum. Climate estimates from TraCE-21ka have been downsampled in space and time and low-pass filtered to match the temporal characteristics of the fossil pollen abundances. Uncertainties for β and breakpoints and permutation tests comparing these parameters are reported in the Supplementary Information (Table S1, Table S4 - S5).

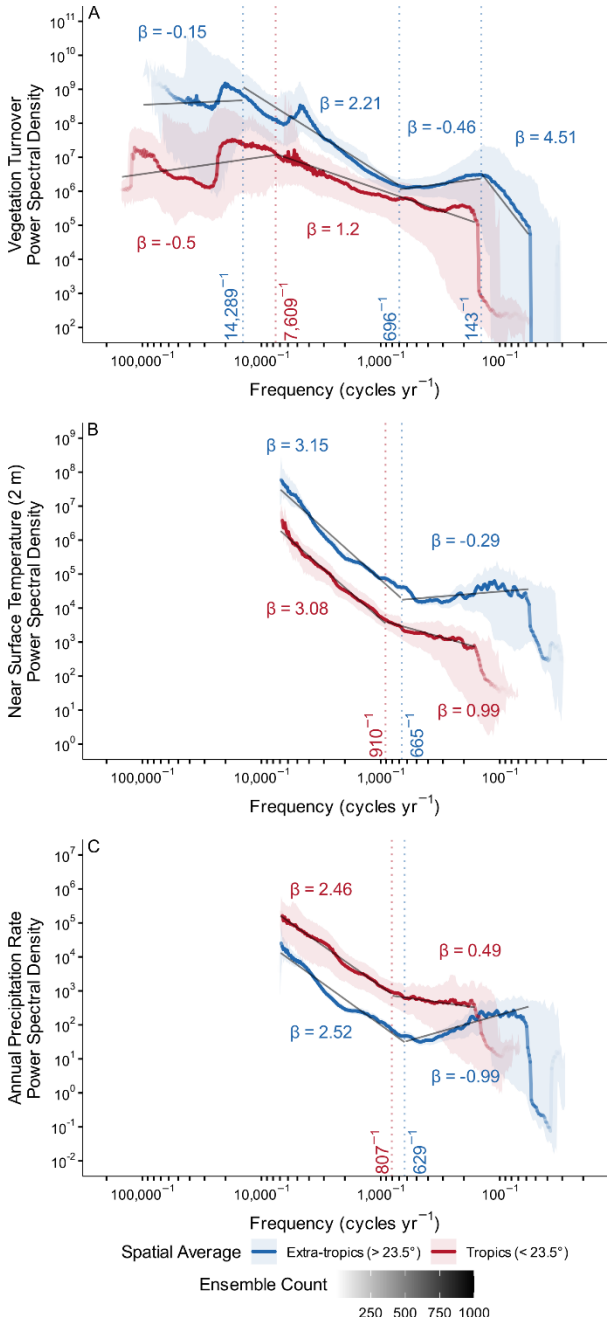

Figure 3. The continuum of (A) vegetation turnover, (B) near-surface temperature, and (C) annual precipitation rate variability, averaged for the extra-tropics (blue, > 23.5°) and tropics (red, < 23.5°) based on the median from an ensemble of spectral power estimates. Power spectra line opacity indicates the number of ensemble members that resolve each frequency. β in the

high frequency band was fit to the maximum frequency that yielded an unbiased estimate (Supplementary Information). Vertical dashed lines correspond to breakpoints identified in the spectral continuum and are colored by the corresponding spatial average. All climate estimates are from TraCE-21ka and have been downsampled as in Figure 1. Uncertainties for β and breakpoints and permutation tests comparing these parameters are reported in the Supplementary Information (Table S1, Table S6 - S9).

References

1. J. Overpeck, C. Whitlock, B. Huntley, "Terrestrial Biosphere Dynamics in the Climate System: Past and Future" in *Paleoclimate, Global Change and the Future*, K. D. Alverson, T. F. Pedersen, R. S. Bradley, Eds. (Springer, Berlin, Heidelberg, 2003; https://doi.org/10.1007/978-3-642-55828-3_5)*Global Change — The IGBP Series*, pp. 81–103.

2. E. M. Wolkovich, B. I. Cook, K. K. McLauchlan, T. J. Davies, Temporal ecology in the Anthropocene. *Ecology Letters* **17**, 1365–1379 (2014).

3. D. Jablonski, Biotic interactions and macroevolution: extensions and mismatches across scales and levels. *Evolution* **62**, 715–739 (2008).

4. R. E. Ricklefs, Community Diversity: Relative Roles of Local and Regional Processes. *Science* **235**, 167–171 (1987).

5. H. R. Delcourt, P. A. Delcourt, Quaternary landscape ecology: Relevant scales in space and time. *Landscape Ecol* **2**, 23–44 (1988).

6. P. F. McDowell, T. Webb, P. J. Bartlein, "Long-Term Environmental Change" in *Ecological Time Series*, T. M. Powell, J. H. Steele, Eds. (Springer US, Boston, MA, 1995; https://doi.org/10.1007/978-1-4615-1769-6_16), pp. 327–370.

7. A. S. Mori, T. Sasaki, M. Kagami, T. Miki, M. Yasuhara, "Feedbacks Between Biodiversity and Climate Change" in *The Ecological and Societal Consequences of Biodiversity Loss* (John Wiley & Sons, Ltd, 2022; https://onlinelibrary.wiley.com/doi/abs/10.1002/9781119902911.ch13), pp. 281–304.

8. M. Yasuhara, R. Danovaro, Temperature impacts on deep-sea biodiversity. *Biological Reviews* **91**, 275–287 (2016).

9. P. Huybers, W. Curry, Links between annual, Milankovitch and continuum temperature variability. *Nature* **441**, 329–332 (2006).

10. F. Zhu, J. Emile-Geay, N. P. McKay, G. J. Hakim, D. Khider, T. R. Ault, E. J. Steig, S. Dee, J. W. Kirchner, Climate models can correctly simulate the continuum of global-average temperature variability. *Proceedings of the National Academy of Sciences* **116**, 8728–8733 (2019).

11. J. W. Williams, E. C. Grimm, J. L. Blois, D. F. Charles, E. B. Davis, S. J. Goring, R. W. Graham, A. J. Smith, M. Anderson, J. Arroyo-Cabrales, A. C. Ashworth, J. L. Betancourt, B. W. Bills, R. K. Booth, P. I. Buckland, B. B. Curry, T. Giesecke, S. T. Jackson, C. Latorre, J. Nichols, T. Purdum, R. E. Roth, M. Stryker, H. Takahara, The Neotoma Paleoecology Database, a multiproxy, international, community-curated data resource. *Quaternary Research* **89**, 156–177 (2018).

12. J. Smith, M. C. Rillo, Á. T. Kocsis, M. Dornelas, D. Fastovich, H.-H. M. Huang, L. Jonkers, W. Kiessling, Q. Li, L. H. Liow, M. Margulis-Ohnuma, S. Meyers, L. Na, A. M. Penny, K. Pippenger, J. Renaudie, E. E. Saupe, M. J. Steinbauer, M. Sugawara, A. Tomašovỳch, J. W. Williams, M. Yasuhara, S. Finnegan, P. M. Hull, BioDeepTime: A database of biodiversity time series for modern and fossil assemblages. *Global Ecology and Biogeography* **n/a** (2023).

13. T. Webb, Is vegetation in equilibrium with climate? How to interpret late-Quaternary pollen data. *Vegetatio* **67**, 75–91 (1986).

14. J. W. Williams, A. Ordonez, J.-C. Svenning, A unifying framework for studying and managing climate-driven rates of ecological change. *Nat Ecol Evol* **5**, 17–26 (2021).

15. J.-C. Svenning, B. Sandel, Disequilibrium vegetation dynamics under future climate change. *American Journal of Botany* **100**, 1266–1286 (2013).

16. M. V. Talluto, I. Boulangeat, S. Vissault, W. Thuiller, D. Gravel, Extinction debt and colonization credit delay range shifts of eastern North American trees. *Nat Ecol Evol* **1**, 1–6 (2017).

17. R. Bertrand, J. Lenoir, C. Piedallu, G. Riofrío-Dillon, P. de Ruffray, C. Vidal, J.-C. Pierrat, J.-C. Gégout, Changes in plant community composition lag behind climate warming in lowland forests. *Nature* **479**, 517–520 (2011).

18. B. J. Butterfield, R. S. Anderson, C. A. Holmgren, J. L. Betancourt, Extinction debt and delayed colonization have had comparable but unique effects on plant community–climate lags since the Last Glacial Maximum. *Global Ecology and Biogeography* **28**, 1067–1077 (2019).

19. R. Spake, M. P. Barajas-Barbosa, S. A. Blowes, D. E. Bowler, C. T. Callaghan, M. Garbowski, S. D. Jurburg, R. van Klink, L. Korell, E. Ladouceur, R. Rozzi, D. S. Viana, W.-B. Xu, J. M. Chase, Detecting Thresholds of Ecological Change in the Anthropocene. *Annual Review of Environment and Resources* **47**, 797–821 (2022).

20. S. R. Carpenter, O. Kinne, *Regime Shifts in Lake Ecosystems : Pattern and Variation* (Ecology Institute, Oldendorf/Luhe, Germany, 2003)*Excellence in ecology*,.

21. Intergovernmental Panel On Climate Change (Ipcc), *Climate Change 2021 – The Physical Science Basis: Working Group I Contribution to the Sixth Assessment Report of the Intergovernmental Panel on Climate Change* (Cambridge University Press, ed. 1, 2023; https://www.cambridge.org/core/product/identifier/9781009157896/type/book).

22. D. J. Thomson, Spectrum estimation and harmonic analysis. *Proceedings of the IEEE* **70**, 1055–1096 (1982).

23. R. Hébert, U. Herzschuh, T. Laepple, Millennial-scale climate variability over land overprinted by ocean temperature fluctuations. *Nat. Geosci.*, 1–7 (2022).

24. P. Yiou, E. Baert, M. F. Loutre, Spectral analysis of climate data. *Surv Geophys* **17**, 619–663 (1996).

25. C. Wunsch, The spectral description of climate change including the 100 ky energy. *Climate Dynamics* **20**, 353–363 (2003).

26. J. T. Overpeck, T. Webb, I. C. Prentice, Quantitative interpretation of fossil pollen spectra - dissimilarity coefficients and the method of modern analogs. *Quaternary Research* **23**, 87–108 (1985).

27. F. He, *Simulating Transient Climate Evolution of the Last Deglaciation with CCSM 3* (2011)vol. 72.

28. Z. Liu, B. L. Otto-Bliesner, F. He, E. C. Brady, R. Tomas, P. U. Clark, A. E. Carlson, J. Lynch-Stieglitz, W. Curry, E. Brook, D. Erickson, R. Jacob, J. Kutzbach, J. Cheng, Transient Simulation of Last Deglaciation with a New Mechanism for Bølling-Allerød Warming. *Science* **325**, 310–314 (2009).

29. J. Jouzel, V. Masson-Delmotte, O. Cattani, G. Dreyfus, S. Falourd, G. Hoffmann, B. Minster, J. Nouet, J. M. Barnola, J. Chappellaz, H. Fischer, J. C. Gallet, S. Johnsen, M. Leuenberger, L. Loulergue, D. Luethi, H. Oerter, F. Parrenin, G. Raisbeck, D. Raynaud, A. Schilt, J. Schwander, E. Selmo, R. Souchez, R. Spahni, B. Stauffer, J. P. Steffensen, B. Stenni, T. F. Stocker, J. L. Tison, M. Werner, E. W. Wolff, Orbital and Millennial Antarctic Climate Variability over the Past 800,000 Years. *Science* **317**, 793–796 (2007).

30. C. W. Snyder, Evolution of global temperature over the past two million years. *Nature* **538**, 226–228 (2016).

31. T. Platt, K. L. Denman, Spectral Analysis in Ecology. *Annu. Rev. Ecol. Syst.* **6**, 189–210 (1975).

32. M. E. Dillon, H. A. Woods, G. Wang, S. B. Fey, D. A. Vasseur, R. S. Telemeco, K. Marshall, S. Pincebourde, Life in the Frequency Domain: the Biological Impacts of Changes in Climate Variability at Multiple Time Scales. *Integrative and Comparative Biology* **56**, 14–30 (2016).

33. K. Hasselmann, Stochastic climate models Part I. Theory. *Tellus* **28**, 473–485 (1976).

34. S. T. Jackson, J. T. Overpeck, Responses of plant populations and communities to environmental changes of the late Quaternary. *Paleobiology* **26**, 194–220 (2000).

35. M. B. Davis, R. G. Shaw, Range Shifts and Adaptive Responses to Quaternary Climate Change. *Science* **292**, 673–679 (2001).

36. M. Chevalier, B. A. S. Davis, O. Heiri, H. Seppa, B. M. Chase, K. Gajewski, T. Lacourse, R. J. Telford, W. Finsinger, J. Guiot, N. Kuhl, S. Y. Maezumi, J. R. Tipton, V. A. Carter, T. Brussel, L. N. Phelps, A. Dawson, M. Zanon, F. Valle, C. Nolan, A. Mauri, A. de Vernal, K. Izumi, L. Holmstrom, J. Marsicek, S. Goring, P. S. Sommer, M. Chaput, D. Kupriyanov, Pollen-based climate reconstruction techniques for late Quaternary studies. *Earth-Sci. Rev.* **210**, 33 (2020).

37. D. Fastovich, J. M. Russell, S. T. Jackson, T. R. Krause, S. A. Marcott, J. W. Williams, Spatial fingerprint of Younger Dryas cooling and warming in eastern North America. *Geophysical Research Letters* **47**, e2020GL090031 (2020).

38. J. Marsicek, B. N. Shuman, P. J. Bartlein, S. L. Shafer, S. Brewer, Reconciling divergent trends and millennial variations in Holocene temperatures. *Nature* **554**, 92 (2018).

39. P. J. Bartlein, S. P. Harrison, S. Brewer, S. Connor, B. A. S. Davis, K. Gajewski, J. Guiot, T. I. Harrison-Prentice, A. Henderson, O. Peyron, I. C. Prentice, M. Scholze, H. Seppä, B. Shuman, S. Sugita, R. S. Thompson, A. E. Viau, J. Williams, H. Wu, Pollen-based continental climate reconstructions at 6 and 21 ka: a global synthesis. *Climate Dynamics* **37**, 775–802 (2011).

40. G. M. Locosselli, R. J. W. Brienen, M. de S. Leite, M. Gloor, S. Krottenthaler, A. A. de Oliveira, J. Barichivich, D. Anhuf, G. Ceccantini, J. Schöngart, M. Buckeridge, Global tree-ring analysis reveals rapid decrease in tropical tree longevity with temperature. *Proceedings of the National Academy of Sciences* **117**, 33358–33364 (2020).

41. R. Rauschkolb, Z. Li, S. Godefroid, L. Dixon, W. Durka, M. Májeková, O. Bossdorf, A. Ensslin, J. F. Scheepens, Evolution of plant drought strategies and herbivore tolerance after two decades of climate change. *New Phytologist* **235**, 773–785 (2022).

42. J. W. Williams, J. L. Blois, B. N. Shuman, Extrinsic and intrinsic forcing of abrupt ecological change: case studies from the late Quaternary. *Journal of Ecology* **99**, 664–677 (2011).

43. M. Scheffer, S. H. Hosper, M. L. Meijer, B. Moss, E. Jeppesen, Alternative equilibria in shallow lakes. *Trends in Ecology & Evolution* **8**, 275–279 (1993).

44. M. Scheffer, S. Carpenter, J. A. Foley, C. Folke, B. Walker, Catastrophic shifts in ecosystems. *Nature* **413**, 591–596 (2001).

45. S. C. Brown, T. M. L. Wigley, B. L. Otto-Bliesner, C. Rahbek, D. A. Fordham, Persistent Quaternary climate refugia are hospices for biodiversity in the Anthropocene. *Nat Clim Change* **10**, 244-+ (2020).

46. H.-B. Fredriksen, K. Rypdal, Spectral Characteristics of Instrumental and Climate Model Surface Temperatures. *Journal of Climate* **29**, 1253–1268 (2016).

47. V. M. R. Muggeo, Estimating regression models with unknown break-points. *Statistics in Medicine* **22**, 3055–3071 (2003).

48. T. Laepple, E. Ziegler, N. Weitzel, R. Hébert, B. Ellerhoff, P. Schoch, B. Martrat, O. Bothe, E. Moreno-Chamarro, M. Chevalier, A. Herbert, K. Rehfeld, Regional but not global temperature variability underestimated by climate models at supradecadal timescales. *Nat. Geosci.* **16**, 958–966 (2023).

49. J. W. Williams, D. M. Post, L. C. Cwynar, A. F. Lotter, A. J. Levesque, Rapid and widespread vegetation responses to past climate change in the North Atlantic region. *Geology* **30**, 971–974 (2002).

50. J. W. Williams, Variations in tree cover in North America since the last glacial maximum. *Global and Planetary Change* **35**, 1–23 (2003).

51. L. C. Peterson, G. H. Haug, K. A. Hughen, U. Röhl, Rapid Changes in the Hydrologic Cycle of the Tropical Atlantic During the Last Glacial. *Science* **290**, 1947–1951 (2000).

52. C. Buizert, V. Gkinis, J. P. Severinghaus, F. He, B. S. Lecavalier, P. Kindler, M. Leuenberger, A. E. Carlson, B. Vinther, V. Masson-Delmotte, J. W. C. White, Z. Liu, B. Otto-Bliesner, E. J. Brook, Greenland temperature response to climate forcing during the last deglaciation. *Science* **345**, 1177–1180 (2014).

53. B. N. Shuman, P. Newby, J. P. Donnelly, Abrupt climate change as an important agent of ecological change in the Northeast U.S. throughout the past 15,000 years. *Quaternary Science Reviews* **28**, 1693–1709 (2009).

54. A. W. Seddon, M. Macias-Fauria, K. J. Willis, Climate and abrupt vegetation change in Northern Europe since the last deglaciation. *The Holocene* **25**, 25–36 (2015).

55. D. Fastovich, J. M. Russell, S. T. Jackson, J. W. Williams, Deglacial temperature controls on no-analog community establishment in the Great Lakes Region. *Quaternary Science Reviews* **234**, 106245 (2020).

56. R. Hébert, L. Schild, T. Laepple, U. Herzschuh, Biome- and timescale-dependence of Holocene vegetation variability in the Northern Hemisphere. *Ecology and Evolution* **13**, e10585 (2023).

57. S. T. Jackson, "Pollen and spores in Quaternary lake sediments as sensors of vegetation composition: theoretical models and empirical evidence" in *Sedimentation of Organic Particles*, A. Traverse, Ed. (Cambridge University Press, Cambridge, 1994; https://www.cambridge.org/core/books/sedimentation-of-organic-particles/pollen-and-spores-in-quaternary-lake-sediments-as-sensors-of-vegetation-composition-theoretical-models-and-empirical-evidence/DCC368064032C32E792D2BBB291EFA36), pp. 253–286.

58. R. Hébert, K. Rehfeld, T. Laepple, Comparing estimation techniques for temporal scaling in palaeoclimate time series. *Nonlinear Processes in Geophysics* **28**, 311–328 (2021).

59. H. D. Grissino-Mayer, H. C. Fritts, The International Tree-Ring Data Bank: an enhanced global database serving the global scientific community. *The Holocene* **7**, 235–238 (1997).

60. S. Zhao, N. Pederson, L. D'Orangeville, J. HilleRisLambers, E. Boose, C. Penone, B. Bauer, Y. Jiang, R. D. Manzanedo, The International Tree-Ring Data Bank (ITRDB) revisited: Data availability and global ecological representativity. *Journal of Biogeography* **46**, 355–368 (2019).

61. O. Mottl, S. G. A. Flantua, K. P. Bhatta, V. A. Felde, T. Giesecke, S. Goring, E. C. Grimm, S. Haberle, H. Hooghiemstra, S. Ivory, P. Kuneš, S. Wolters, A. W. R. Seddon, J. W. Williams, Global acceleration in rates of vegetation change over the past 18,000 years. *Science* **372**, 860–864 (2021).

62. L. Stephens, D. Fuller, N. Boivin, T. Rick, N. Gauthier, A. Kay, B. Marwick, C. G. Armstrong, C. M. Barton, T. Denham, K. Douglass, J. Driver, L. Janz, P. Roberts, J. D. Rogers, H. Thakar, M. Altaweel, A. L. Johnson, M. M. Sampietro Vattuone, M. Aldenderfer, S. Archila, G. Artioli, M. T. Bale, T. Beach, F. Borrell, T. Braje, P. I. Buckland, N. G. Jiménez Cano, J. M. Capriles, A. Diez Castillo, Ç. Çilingiroğlu, M. Negus Cleary, J. Conolly, P. R. Coutros, R. A. Covey, M. Cremaschi, A. Crowther, L. Der, S. di Lernia, J. F. Doershuk, W. E. Doolittle, K. J. Edwards, J. M. Erlandson, D. Evans, A. Fairbairn, P. Faulkner, G. Feinman, R. Fernandes, S. M. Fitzpatrick, R. Fyfe, E. Garcea, S. Goldstein, R. C. Goodman, J. Dalpoim Guedes, J. Herrmann, P. Hiscock, P. Hommel, K. A. Horsburgh, C. Hritz, J. W. Ives, A. Junno, J. G. Kahn, B. Kaufman, C. Kearns, T. R. Kidder, F. Lanoë, D. Lawrence, G.-A. Lee, M. J. Levin, H. B. Lindskoug, J. A. López-Sáez, S. Macrae, R. Marchant, J. M. Marston, S. McClure, M. D. McCoy, A. V. Miller, M. Morrison, G. Motuzaite Matuzeviciute, J. Müller, A. Nayak, S. Noerwidi, T. M. Peres, C. E. Peterson, L. Proctor, A. R. Randall, S. Renette, G. Robbins Schug, K. Ryzewski, R. Saini, V. Scheinsohn, P. Schmidt, P. Sebillaud, O. Seitsonen, I. A. Simpson, A. Sołtysiak, R. J. Speakman, R. N. Spengler, M. L. Steffen, M. J. Storozum, K. M. Strickland, J. Thompson, T. L. Thurston, S. Ulm, M. C. Ustunkaya, M. H. Welker, C. West, P. R. Williams, D. K. Wright, N. Wright, M. Zahir, A. Zerboni, E. Beaudoin, S. Munevar Garcia, J. Powell, A. Thornton, J. O. Kaplan, M.-J. Gaillard, K. Klein Goldewijk, E. Ellis, Archaeological assessment reveals Earth's early transformation through land use. *Science* **365**, 897–902 (2019).

63. K. Zhu, C. W. Woodall, J. S. Clark, Failure to migrate: lack of tree range expansion in response to climate change. *Global Change Biology* **18**, 1042–1052 (2012).

64. M. Mudelsee, M. E. Raymo, Slow dynamics of the Northern Hemisphere glaciation. *Paleoceanography* **20** (2005).

65. S. R. Meyers, L. A. Hinnov, Northern Hemisphere glaciation and the evolution of Plio-Pleistocene climate noise. *Paleoceanography* **25** (2010).

66. S. Ferrier, G. Manion, J. Elith, K. Richardson, Using generalized dissimilarity modelling to analyse and predict patterns of beta diversity in regional biodiversity assessment. *Diversity and Distributions* **13**, 252–264 (2007).

67. G. Bond, W. Showers, M. Cheseby, R. Lotti, P. Almasi, P. deMenocal, P. Priore, H. Cullen, I. Hajdas, G. Bonani, A pervasive millennial-scale cycle in North Atlantic Holocene and glacial climates. Science 278, 1257–1266 (1997).

68. B. Huntley, J. R. M. Allen, Y. C. Collingham, T. Hickler, A. M. Lister, J. Singarayer, A. J. Stuart, M. T. Sykes, P. J. Valdes, Millennial climatic fluctuations are key to the structure of last glacial ecosystems. *PloS one* **8** (2013).

69. H. Wanner, J. Beer, J. Butikofer, T. J. Crowley, U. Cubasch, J. Fluckiger, H. Goosse, M. Grosjean, F. Joos, J. O. Kaplan, M. Kuttel, S. A. Muller, I. C. Prentice, O. Solomina, T. F. Stocker, P. Tarasov, M. Wagner, M. Widmann, Mid- to Late Holocene climate change: an overview. *Quaternary Science Reviews* **27**, 1791–1828 (2008).

70. D. Magri, Patterns of post-glacial spread and the extent of glacial refugia of European beech (Fagus sylvatica). *Journal of Biogeography* **35**, 450–463 (2008).

71. M. G. Turner, W. J. Calder, G. S. Cumming, T. P. Hughes, A. Jentsch, S. L. LaDeau, T. M. Lenton, B. N. Shuman, M. R. Turetsky, Z. Ratajczak, J. W. Williams, A. P. Williams, S. R. Carpenter, Climate change, ecosystems and abrupt change: science priorities. *Philosophical Transactions of the Royal Society B: Biological Sciences* **375**, 20190105 (2020).

72. T. M. Lenton, J. Rockström, O. Gaffney, S. Rahmstorf, K. Richardson, W. Steffen, H. J. Schellnhuber, Climate tipping points — too risky to bet against. *Nature* **575**, 592–595 (2019).

73. R. R. Nemani, C. D. Keeling, H. Hashimoto, W. M. Jolly, S. C. Piper, C. J. Tucker, R. B. Myneni, S. W. Running, Climate-Driven Increases in Global Terrestrial Net Primary Production from 1982 to 1999. *Science* **300**, 1560–1563 (2003).

74. D. Fastovich, Code and Data for Timescale-dependent response of vegetation to climate change, version 1.0, Zenodo (2024); https://doi.org/10.5281/ZENODO.12726798.

75. M. B. Davis, "Quaternary history and the stability of forest communities" in *Forest Succession: Concepts and Application*, D. C. West, H. H. Shugart, D. B. Botkin, Eds. (Springer New York, New York, NY, 1981; https://doi.org/10.1007/978-1-4612-5950-3_10), pp. 132–153.

76. D. R. Foster, D. H. Knight, J. F. Franklin, Landscape Patterns and Legacies Resulting from Large, Infrequent Forest Disturbances. *Ecosystems* **1**, 497–510 (1998).

77. L. B. Brubaker, Responses of tree populations to climatic change. *Vegetatio* **67**, 119–130 (1986).

78. T. Webb, S. E. Howe, R. H. W. Bradshaw, K. M. Heide, Estimating plant abundances from pollen percentages: The use of regression analysis. *Review of Palaeobotany and Palynology* **34**, 269–300 (1981).

79. A. Parnell, Bchron: Radiocarbon dating, age-depth modelling, relative sea level rate estimation, and non-parametric phase modelling. *R package version* **4** (2014).

80. A. C. Parnell, J. Sweeney, T. K. Doan, M. Salter-Townshend, J. R. M. Allen, B. Huntley, J. Haslett, Bayesian inference for palaeoclimate with time uncertainty and stochastic volatility, *Journal of the Royal Statistical Society: Series C (Applied Statistics)*. **64** (2014)pp. 115–138.

81. P. J. Reimer, W. E. N. Austin, E. Bard, A. Bayliss, P. G. Blackwell, C. B. Ramsey, M. Butzin, H. Cheng, R. L. Edwards, M. Friedrich, P. M. Grootes, T. P. Guilderson, I. Hajdas, T. J. Heaton, A. G. Hogg, K. A. Hughen, B. Kromer, S. W. Manning, R. Muscheler, J. G. Palmer, C. Pearson, J. van der Plicht, R. W. Reimer, D. A. Richards, E. M. Scott, J. R. Southon, C. S. M. Turney, L. Wacker, F. Adolphi, U. Büntgen, M. Capano, S. M. Fahrni, A. Fogtmann-Schulz, R. Friedrich, P. Köhler, S. Kudsk, F. Miyake, J. Olsen, F. Reinig, M. Sakamoto, A. Sookdeo, S. Talamo, The IntCal20 Northern Hemisphere Radiocarbon Age Calibration Curve (0–55 cal kBP). *Radiocarbon* **62**, 725–757 (2020).

82. A. G. Hogg, T. J. Heaton, Q. Hua, J. G. Palmer, C. S. Turney, J. Southon, A. Bayliss, P. G. Blackwell, G. Boswijk, C. B. Ramsey, C. Pearson, F. Petchey, P. Reimer, R. Reimer, L. Wacker, SHCal20 Southern Hemisphere Calibration, 0–55,000 Years cal BP. *Radiocarbon* **62**, 759–778 (2020).

83. S. G. A. Flantua, O. Mottl, K. P. Bhatta, V. A. Felde, T. Giesecke, S. J. Goring, E. C. Grimm, S. G. Haberle, H. Hooghiemstra, S. J. Ivory, P. Kuneš, S. Wolters, A. W. R. Seddon, J. W. Williams, Mottl et al. (2021, Science) Taxonomic harmonization tables for North America, Latin America, Europe, Asia, Africa, figshare (2021); https://doi.org/10.6084/m9.figshare.13049735.v2.

84. F. Biondi, D. M. Meko, G. Piovesan, Maximum tree lifespans derived from public-domain dendrochronological data. *iScience* **26**, 106138 (2023).

85. S. R. Meyers, “Astrochron: An R package for astrochronology” (manual, 2014); https://cran.r-project.org/package=astrochron.

86. R Core Team, “R: A language and environment for statistical computing” (manual, Vienna, Austria, 2021); https://www.R-project.org/.

87. J. C. Gower, Some distance properties of latent root and vector methods used in multivariate analysis. *Biometrika* **53**, 325–338 (1966).

88. D. G. Gavin, W. W. Oswald, E. R. Wahl, J. W. Williams, A statistical approach to evaluating distance metrics and analog assignments for pollen records. *Quaternary Research* **60**, 356–367 (2003).

89. T. Laepple, P. Huybers, Reconciling discrepancies between Uk37 and Mg/Ca reconstructions of Holocene marine temperature variability. *Earth and Planetary Science Letters* **375**, 418–429 (2013).

90. J. W. Kirchner, Aliasing in $1⁄{f}^{\ensuremath{\alpha}}$ noise spectra: Origins, consequences, and remedies. *Phys. Rev. E* **71**, 066110 (2005).

91. M. E. Mann, J. M. Lees, Robust estimation of background noise and signal detection in climatic time series. *Climatic Change* **33**, 409–445 (1996).

92. S. Coats, J. E. Smerdon, S. Stevenson, J. T. Fasullo, B. Otto-Bliesner, T. R. Ault, Paleoclimate Constraints on the Spatiotemporal Character of Past and Future Droughts. *Journal of Climate* **33**, 9883–9903 (2020).

93. S. Minobe, A 50–70 year climatic oscillation over the North Pacific and North America. *Geophysical Research Letters* **24**, 683–686 (1997).

94. D. I. Vyushin, P. J. Kushner, Power-Law and Long-Memory Characteristics of the Atmospheric General Circulation. *Journal of Climate* **22**, 2890–2904 (2009).

95. J. M. Lora, D. E. Ibarra, The North American hydrologic cycle through the last deglaciation. *Quaternary Science Reviews* **226**, 25 (2019).

96. S. A. Marcott, P. U. Clark, L. Padman, G. P. Klinkhammer, S. R. Springer, Z. Y. Liu, B. L. Otto-Bliesner, A. E. Carlson, A. Ungerer, J. Padman, F. He, J. Cheng, A. Schmittner, Ice-shelf collapse from subsurface warming as a trigger for Heinrich events. *Proceedings of the National Academy of Sciences of the United States of America* **108**, 13415–13419 (2011).

97. F. He, J. D. Shakun, P. U. Clark, A. E. Carlson, Z. Y. Liu, B. L. Otto-Bliesner, J. E. Kutzbach, Northern Hemisphere forcing of Southern Hemisphere climate during the last deglaciation. *Nature* **494**, 81–85 (2013).

98. R. F. Ivanovic, L. J. Gregoire, A. Burke, A. D. Wickert, P. J. Valdes, H. C. Ng, L. F. Robinson, J. F. McManus, J. X. Mitrovica, L. Lee, J. E. Dentith, Acceleration of Northern Ice Sheet Melt Induces AMOC Slowdown and Northern Cooling in Simulations of the Early Last Deglaciation. *Paleoceanogr. Paleoclimatology* **33**, 807–824 (2018).

99. S. A. Marcott, T. K. Bauska, C. Buizert, E. J. Steig, J. L. Rosen, K. M. Cuffey, T. J. Fudge, J. P. Severinghaus, J. Ahn, M. L. Kalk, J. R. McConnell, T. Sowers, K. C. Taylor, J. W. C. White, E. J. Brook, Centennial-scale changes in the global carbon cycle during the last deglaciation. *Nature* **514**, 616 (2014).

100. E. Monnin, A. Indermühle, A. Dällenbach, J. Flückiger, B. Stauffer, T. F. Stocker, D. Raynaud, J.-M. Barnola, Atmospheric CO2 Concentrations over the Last Glacial Termination. *Science* **291**, 112–114 (2001).

101. S. C. Brown, C. Mellin, J. García Molinos, E. D. Lorenzen, D. A. Fordham, Faster ocean warming threatens richest areas of marine biodiversity. *Global Change Biology* **28**, 5849–5858 (2022).

102. D. A. Fordham, F. Saltré, S. Haythorne, T. M. L. Wigley, B. L. Otto-Bliesner, K. C. Chan, B. W. Brook, PaleoView: a tool for generating continuous climate projections spanning the last 21 000 years at regional and global scales. *Ecography* **40**, 1348–1358 (2017).

103. J. R. Petit, J. Jouzel, D. Raynaud, N. I. Barkov, J.-M. Barnola, I. Basile, M. Bender, J. Chappellaz, M. Davis, G. Delaygue, M. Delmotte, V. M. Kotlyakov, M. Legrand, V. Y. Lipenkov, C. Lorius, L. PÉpin, C. Ritz, E. Saltzman, M. Stievenard, Climate and atmospheric history of the past 420,000 years from the Vostok ice core, Antarctica. *Nature* **399**, 429–436 (1999).

104. C. Barbante, J.-M. Barnola, S. Becagli, J. Beer, M. Bigler, C. Boutron, T. Blunier, E. Castellano, O. Cattani, J. Chappellaz, D. Dahl-Jensen, M. Debret, B. Delmonte, D. Dick, S. Falourd, S. Faria, U. Federer, H. Fischer, J. Freitag, A. Frenzel, D. Fritzsche, F. Fundel, P. Gabrielli, V. Gaspari, R. Gersonde, W. Graf, D. Grigoriev, I. Hamann, M. Hansson, G. Hoffmann, M. A. Hutterli, P. Huybrechts, E. Isaksson, S. Johnsen, J. Jouzel, M. Kaczmarska, T. Karlin, P. Kaufmann, S. Kipfstuhl, M. Kohno, F. Lambert, A. Lambrecht, A. Lambrecht, A. Landais, G. Lawer, M. Leuenberger, G. Littot, L. Loulergue, D. Lüthi, V. Maggi, F. Marino, V. Masson-Delmotte, H. Meyer, H. Miller, R. Mulvaney, B. Narcisi, J. Oerlemans, H. Oerter, F. Parrenin, J.-R. Petit, G. Raisbeck, D. Raynaud, R. Röthlisberger, U. Ruth, O. Rybak, M. Severi, J. Schmitt, J. Schwander, U. Siegenthaler, M.-L. Siggaard-Andersen, R. Spahni, J. P. Steffensen, B. Stenni, T. F. Stocker, J.-L. Tison, R. Traversi, R. Udisti, F. Valero-Delgado, M. R. van den Broeke, R. S. W. van de Wal, D. Wagenbach, A. Wegner, K. Weiler, F. Wilhelms, J.-G. Winther, E. Wolff, EPICA Community Members, One-to-one coupling of glacial climate variability in Greenland and Antarctica. *Nature* **444**, 195–198 (2006).

105. D. Kaufman, N. McKay, C. Routson, M. Erb, C. Datwyler, P. S. Sommer, O. Heiri, B. Davis, Holocene global mean surface temperature, a multi-method reconstruction approach. *Scientific Data* **7**, 13 (2020).

106. J. D. Hays, J. Imbrie, N. J. Shackleton, Variations in the Earth's Orbit: Pacemaker of the Ice Ages. *Science* **194**, 1121–1132 (1976).

107. A. Berger, Milankovitch Theory and climate. *Reviews of Geophysics* **26**, 624–657 (1988).

108. W. Zhao, P. E. Tarasov, A. V. Lozhkin, P. M. Anderson, A. A. Andreev, J. A. Korzun, M. Melles, E. Y. Nedorubova, V. Wennrich, High-latitude vegetation and climate changes during the Mid-Pleistocene Transition inferred from a palynological record from Lake El'gygytgyn, NE Russian Arctic. *Boreas* **47**, 137–149 (2018).

109. Y. Zhao, P. C. Tzedakis, Q. Li, F. Qin, Q. Cui, C. Liang, H. J. B. Birks, Y. Liu, Z. Zhang, J. Ge, H. Zhao, V. A. Felde, C. Deng, M. Cai, H. Li, W. Ren, H. Wei, H. Yang, J. Zhang, Z. Yu, Z. Guo, Evolution of vegetation and climate variability on the Tibetan Plateau over the past 1.74 million years. *Science Advances* **6**, eaay6193 (2020).

110. P. C. Tzedakis, Long-term tree populations in northwest Greece through multiple Quaternary climatic cycles. *Nature* **364**, 437–440 (1993).

111. A. L. Berger, Long-Term Variations of Caloric Insolation Resulting from the Earth's Orbital Elements1. *Quaternary Research* **9**, 139–167 (1978).

112. J. Imbrie, A. Berger, E. A. Boyle, S. C. Clemens, A. Duffy, W. R. Howard, G. Kukla, J. Kutzbach, D. G. Martinson, A. McIntyre, A. C. Mix, B. Molfino, J. J. Morley, L. C. Peterson, N. G. Pisias, W. L. Prell, M. E. Raymo, N. J. Shackleton, J. R. Toggweiler, On the structure and origin of major glaciation cycles 2. The 100,000-year cycle. *Paleoceanography* **8**, 699–735 (1993).

113. C. J. F. ter Braak, Canonical Correspondence Analysis: A New Eigenvector Technique for Multivariate Direct Gradient Analysis. *Ecology* **67**, 1167–1179 (1986).

114. D. B. Percival, A. T. Walden, *Spectral Analysis for Physical Applications* (Cambridge University Press, ed. 1, 1993; https://www.cambridge.org/core/product/identifier/9780511622762/type/book).

115. E. C. Ellis, J. O. Kaplan, D. Q. Fuller, S. Vavrus, K. Klein Goldewijk, P. H. Verburg, Used planet: A global history. *Proceedings of the National Academy of Sciences* **110**, 7978–7985 (2013).

Supplemental Information

Methods

Fossil Pollen Abundances and Age Depth Modeling

We estimate vegetation turnover from fossil pollen abundances stored in geologic archives, such as lacustrine sediments (*36*). Fossil pollen tracks plant assemblage composition through time, albeit with some biases and limitations. Taxonomic resolution is often to the genus level (e.g. *Picea*), though species-level identification is possible (e.g. *Alnus rugosa*) for some fossil pollen morphotypes, and only family-level identification is possible for others (e.g. Poaceae). Additionally, some taxa overproduce pollen and others underproduce pollen relative to the source vegetation assemblage. For instance, pine (*Pinus*) is often overrepresented in pollen assemblages while fir (*Abies*) tends to be underrepresented (*78*). Our analyses account for these production biases by including metrics that downweigh abundant fossil pollen taxa and increase the weight of rarer taxa (e.g. squared chord dissimilarity metric incorporates a square root transform and we square root transform the fossil pollen assemblages before correspondence analysis). When these biases are considered and accounted for in analyses, as we do here, fossil pollen is an effective representation of the source plant assemblage. We refer the reader to Chevalier et al. (*36*) for a comprehensive review of fossil pollen as a proxy for plant assemblage composition.

We gathered fossil pollen abundance data from the Neotoma Paleoecology Database (*11*) in May 2022, which was included as a part of the BioDeepTime database (*12*). For this fossil pollen data aggregation, we searched all fossil pollen records in Neotoma with at least 10 fossil pollen

assemblages through time. Our initial search was based on the site list from Mottl et al. (*61*), which compiled 1,181 high-quality fossil pollen records from Neotoma that met our requirements. However, we did not temporally limit our search to 18,000 years as in Mottl et al. (*61*), which produced an additional 181 fossil pollen records, hereafter referred to as "sites". Note, however, that in Neotoma, one site-level sedimentary archive may have multiple fossil pollen records (e.g. if there are multiple cores from a lake or mire). In total, we compiled 1,362 sites with at least 10 observations of a fossil pollen assemblage through time (e.g. at least 10 points in each assemblage time series).

We created age-depth models using Bchron (*79*, *80*) to improve upon existing Neotoma age estimates, which sometimes rely on age-depth models that can underestimate error. Bchron uses information from sparse but specific ages for depths in sedimentary archives for the sites to develop a continuous model of sedimentation from which ages at every depth can be estimated (*80*). An ensemble of possible sedimentation rates is estimated from the chronological controls to generate a posterior distribution of age-depth relationships that allows uncertainty about the age-depth relationship in a sedimentary archive to be propagated to all analyses. Age controls included radiocarbon years, varve years, biostratigraphic markers, and core-top age.

Bchron models were run with default parameters (*80*), except for the radiocarbon calibration curve, which requires hemisphere-specificity to convert radiocarbon years to calendar years due to interhemispheric differences in $^{14}CO_2$ production, uptake, and reservoir effects. Sites in the Northern Hemisphere were calibrated using IntCal20 (*81*) and sites in the Southern Hemisphere were calibrated using SHCal20 (*82*). Non-radiocarbon ages were incorporated into Bchron as calendar years before 1950, with Gaussian errors. Chronological controls with no given age uncertainties, often the case with biostratigraphic ages, were assigned a Gaussian, one standard deviation, age error that was 10% of the age estimate (e.g. for an age estimate of 1,000 years with no assigned error, the ages followed a N(1000, 100^2) distribution in Bchron). From our compilation, 19 sites had only one chronological control and were excluded from further analyses. Additionally, Bchron failed to initialize for five sites that were also excluded.

After creating new age-depth models, we harmonized the taxonomy across these sites using taxa lists from Flantua et al. (*83*). We were not able to match taxa in Flantua et al. (*83*) for 21 sites, so these sites were removed from further analyses. Of these removed sites, 16 were in Oceania and Australia because the taxonomy harmonization lists from Flantua et al. (*83*) do not include these regions (Table S2). Lastly, one site (Foy Lake, Table S2) contained negative abundances for some fossil pollen counts and was removed from further analyses. Five sites had issues with both chronological controls and taxonomy harmonization, therefore the final compilation of fossil pollen abundances included 1,321 datasets with good spatiotemporal coverage (Table S2). Sites span the Southern Hemisphere midlatitudes to the Northern Hemisphere Arctic, with the densest sampling between 40° N and 50° N, and the least dense sampling between 20° S and 50° S (Figure S6). The Northern Hemisphere is better represented across sites than the Southern Hemisphere. Temporally, these records span the last 600,000 years, with one site spanning an interval from 1.4 to 1.5 Ma, and they are heavily concentrated in the last 20,000 years (Figure S6). Based on the median age-depth model for each site, 389 sites have a temporal span less than 10,000 years, 746 sites have a temporal span between 10,000 to 20,000 years, 72 have a temporal span between 20,000 to 30,000 years, 43 have a temporal span between 30,000 to 40,000 years,

17 have a temporal span between 40,000 to 50,000 years, 19 have a temporal span between 50,000 to 60,000 years, seven have a temporal span between 60,000 to 70,000 years, six have a temporal span between 70,000 to 80,000 years, three have a temporal span between 80,000 to 90,000 years, one has a temporal span between 90,000 to 100,000 years, and 18 have a temporal span greater than 100,000 years. Of this final compilation, seven sites had different fossil pollen assemblages at identical depths (Dataset IDs: 22,636, 22,759, 3,973, 4,196, 4,197, 4,7595, 525 in Table S2). For each duplicate depth, we retained the first entry.

Tree Longevity Estimates

We estimated tree longevity with observations from all taxa available in the International Tree Ring Data Bank (ITRDB) (*59*, *60*). We gathered all tree ring width records and retained tree ring collections where at least one tree ring record spanned 90% of the tree-ring collection chronology, to minimize underestimation and overestimation of longevity (*40*). We used the longest tree ring record in a collection to estimate longevity for that collection and report the median across all collections in the main text (*84*). The spatial distribution of the ITRDB is comparable to the fossil pollen sites, which have the greatest density of tree ring width records in North America and Europe and comparatively fewer records in the Southern Hemisphere (Figure S6) (*60*). The ITRDB lacks records in the tropics, but our median estimate of tree longevity (246 years) agrees with a compilation of tree ring width records from the tropics (*40*).

Spectral Analysis

We used Thomson's multitaper method (MTM) (*22*) to estimate the power spectra of fossil pollen turnover using the *astrochron* R-package (R version 4.4.1, *astrochron* version 1.4) (*85*, *86*). MTM is a Fourier-based method that reduces spectral bias (e.g., spectral leakage) through the application of multiple orthogonal data "tapers" that weigh a time series according to Slepian functions (*22*), of which we used five 3π prolate tapers. The application of Slepian data tapers imparts several positive attributes to MTM when compared to the standard discrete Fourier transform: a reduction in spectral leakage and optimal bias protection for a specified bandwidth resolution, and leveraging of the multiple tapers to provide a statistical sample for estimation of spectral power and its uncertainty (*22*). We scale spectral estimates from MTM by energy per unit frequency to return power spectral density, hereafter referred to as the power spectrum (*9*). An underlying assumption in these analyses, and all spectral analyses, is that a single power spectrum is a good representation of the entire time series.

We further processed the fossil pollen abundances to meet the MTM requirements of a univariate, regularly sampled time series. We addressed the requirement of a single time series by using principal coordinate analysis (PCO) (*87*) on fossil pollen dissimilarity matrices to reduce the dimensionality of the fossil pollen abundances. Pollen dissimilarity matrices were calculated for each individual time series using the squared chord distance metric (*26*), which consistently outperforms other distance metrics in distinguishing between two distinct fossil pollen assemblages (*26*, *88*). We retained the primary (PCO1) and secondary (PCO2) dimensions of variability for further analysis via MTM and presented the results from the primary dimension of variability in the main manuscript.

We sought to identify latitudinal differences in fossil pollen dissimilarity, for comparison with climate variables which are known to have a variance structure that varies by latitude (*9*). To that end, we multiplied PCO1 by the square root of its corresponding eigenvalue. This procedure scales PCO1 for each fossil pollen assemblage by the variance explained by that dimension. That is, a fossil pollen assemblage where PCO1 explains a substantial amount of compositional variance will have a large eigenvalue corresponding to PCO1 and PCO1 will be up-weighted, producing high spectral energy across all frequencies. In contrast, a fossil pollen assemblage where PCO1 explains little variance will have a small eigenvalue corresponding to PCO1 and PCO1 will be down-weighted. Total spectral energy (i.e. area under a power spectral density spectrum) is equal to the variance of the time series (Parseval's theorem). Therefore, any spatial patterns in the variance explained by PCO1 are imprinted onto the time series and will produce high spectral power when PCO1 is up-weighted and low spectral power when PCO1 is down-weighted. This effect carries forward to spatially averaged power spectra (i.e. tropical and extra-tropical averaged power spectra) thereby enabling an assessment of whether there are spatial patterns in fossil pollen turnover.

Temporal sampling that is evenly spaced (i.e. identical temporal distance between all consecutive samples) is required by MTM, but this condition is rarely met by proxy data extracted from geologic archives and is not met by any of our fossil pollen sites. Therefore, we interpolated PCO1 of all fossil pollen assemblages using a linear interpolation approach adapted from (*89*). This approach aims to determine an optimal interpolation resolution and minimize energy loss at high frequencies by comparing the PCO1 power spectra to the power spectra of a power law process where $\beta = 1$. The optimal interpolation resolution is identified when the ratio between the theoretical and empirical power spectra crosses 0.7 (*89*). This approach objectively determines an optimal interpolation resolution and includes filtering to minimize the aliasing of high frequency variance that is often present in sedimentary archives (implemented in the new *astrochron* function 'linterpLH13' and present in the Zenodo data repository (*74*)).

We estimated the power spectra of global ecological turnover by performing MTM on PCO1 for individual sites after subtracting the mean from each site-level PCO1 time series, binning spectral power by log10(frequency), and then averaging spectral power across sites within each such bin. This choice was made to avoid convoluting temporal and spatial variance in the eigenvector decomposition of the community dissimilarity matrix, as would have occurred if we considered all sites and samples together. By averaging power spectra across sites, we leverage both short, highly-sampled records to resolve high frequencies and long, sparsely-sampled records to resolve low frequencies - characteristics that would be difficult to achieve using any single site's power spectrum alone. For averaging site-level power spectra, we used a bin size of 0.01 in log10(frequency) coordinates, which equates to $22{,}000^{-1}$ $years^{-1}$ near the smallest frequencies (e.g. $10^{-6} – 10^{-5.99}$ $years^{-1}$) and <1 year near the largest frequencies (e.g. $10^{0.99} – 10^{1}$ $years^{-1}$).

After estimating the spectra of global vegetation turnover we evaluated the continuum of global vegetation turnover for specific frequency bands using an ordinary least squares linear regression in log-log space for frequencies resolved by at least two sites (*9*, *10*). Prior to the regression, we smoothed the spatially averaged power spectra using a Gaussian kernel in log10 frequency coordinates with a width of 0.03 (*23*, *90*). Using the smoothed global estimate of spectral power

for global vegetation turnover, frequency is a predictor of spectral power and the resulting slope is the β exponent in the $S(f) \propto f^{-\beta}$ power law relationship (*9*, *10*). To determine the frequency bands of distinct temporal scaling regimes in spectral power for global vegetation turnover we identified breakpoint locations in the log-log relationship between spectral power and frequency through piecewise linear regressions in the *segmented* R package (version 2.1.2) (*47*). We constrained segmented regressions to identify three breakpoints (low, intermediate, and high frequencies) for fossil pollen turnover and one breakpoint for simulated temperature and precipitation. The number of breakpoints was based on prior expectations for climate (*9*, *10*) and visual inspection for fossil pollen. Although the number of breakpoints is constrained in the segmented regressions, the location of these breakpoints depends on the power spectrum. For vegetation turnover, β was then fit across the four frequency ranges between the three identified breakpoints: (1) the lowest frequency resolved and the low frequency breakpoint, (2) the low frequency breakpoint and the intermediate frequency breakpoint, (3) the intermediate frequency breakpoint and high frequency breakpoint, and (4) the high frequency breakpoint to the highest frequency that produces unbiased estimates of β (see *Estimating the Highest Resolvable Frequency for Spectral Analyses*). For example, if a breakpoint in the log-log relationship between spectral power and frequency was identified at 115^{-1} years^{-1}, 600^{-1} years^{-1}, and $4{,}000^{-1}$ years^{-1}, β was fit between (1) the lowest frequency resolved and $4{,}000^{-1}$ years^{-1}, (2) from $4{,}000^{-1}$ years^{-1} and 600^{-1} years^{-1}, (3) from 600^{-1} years^{-1} to 115 years^{-1}, and (4) from 115 years^{-1} to the highest frequency that produces unbiased estimates of β. For temperature and precipitation, we fit β between the lowest frequency resolved and the one breakpoint identified and again from the one breakpoint identified to the highest frequency that produces unbiased estimates of β.

Recently, methods for estimation of temporal scaling in time series were compared for their ability to reproduce β in synthetic paleoclimate time series with known β and performed reasonably well (*58*). In these analyses, MTM emerged biased towards larger β values when evaluating the full frequency range, compared to other spectral transformation methods (*58*). However, MTM showed little bias at long timescales (greater than nine times the mean resolution), moderate bias at intermediate timescales (greater than 4 times the mean resolution), and generally outperformed competing methods such as spectral transformation from the Lomb-Scargle periodogram when β is high and the input data is irregularly sampled (*58*). Only Haar structure functions more accurately estimated β from the synthetic dataset, but the approach is limited to $-1 < \beta < 3$ (*58*) and does not allow for the identification/influence of quasiperiodic/periodic signals that may bias estimates of the spectral continuum (*91*). Additionally, MTM has seen broad use in paleoclimatology (*9*, *23*, *92*) and atmospheric sciences (*93*, *94*) for estimating β, providing baseline estimates for comparison with our study.

TraCE-21ka and Proxy Paleoclimate Estimates

TraCE-21ka is a series of fully coupled climate model experiments that simulate the effect of transient climate forcings of the most recent deglaciation with the Community Climate System Model, version 3 (*27*, *28*). TraCE-21ka includes transient changes in ice sheet topography, meltwater forcing, orbital configuration, and greenhouse gas concentration that matched then-current proxy reconstructions (*27*, *28*). These climate simulations have been pillars of paleoclimatological research and have undergone substantial comparisons against proxy reconstructions and generally perform well (*27*, *28*, *52*, *95–97*). Unlike proxy-based climate

reconstructions, TraCE-21ka offers full fields that are annually resolved and well-suited for comparison against spectral estimates from fossil pollen.

TraCE-21ka has known deficiencies such as seasonal precipitation biases in North America (*95*) and imperfect greenhouse gas and meltwater forcings (*98–100*). What's more, all climate models overestimate high frequency climate variability and underestimate low frequency climate variability at local and regional scales (*48*), but our low-pass filtering procedure (summarized below) partially mitigates this climate model limitation by reducing high frequency variability. Nonetheless, TraCE-21ka remains the most comprehensive set of paleoclimatic simulations for the last deglaciation, which are widely used to assess ecological relationships to paleoclimate (*45*, *101*, *102*). Recently, the TraCE-21ka experiments were the first climate simulations to show a scaling break in the continuum of mean global temperature that is expected to exist given physical principles (*10*).

We averaged monthly near-surface temperature (2 m) and total precipitation rate into annual averages. We sought to make direct comparisons between power spectra of simulated temperature, simulated precipitation, and vegetation turnover and degraded the TraCE-21ka climate simulation to match the spatial and temporal characteristics of the fossil pollen sites. Specifically, we subsampled TraCE-21ka spatially to get the nearest grid cell for every fossil pollen site and applied a low-pass filter with a characteristic timescale of twice the mean resolution of the corresponding fossil pollen record to guard against aliasing of high-frequency variance (*23*, *58*). We then downsampled these low-pass filtered climate time series temporally, retaining only the years with fossil pollen data. This process produced a dataset of simulated temperature and precipitation that matched fossil pollen abundances in space and time with similar temporal characteristics (i.e. low-pass smoothing induced by sedimentation). Finally, we interpolated the simulated temperature and precipitation to a regular temporal grid using the same methodology applied to the fossil pollen data (*89*). All spectral analyses for TraCE-21ka were performed on these spatiotemporally subsampled and interpolated temperature and precipitation time series.

For subsampling of the TraCE-21ka simulations, we excluded those fossil pollen samples that were outside of the temporal coverage of TraCE-21ka. Fossil pollen sites that did not contain any fossil pollen assemblage observations within the last 21,000 years were excluded and not represented in the spectral estimates of the TraCE-21ka simulations.

To capture climate variability outside of the last 21,000 years we supplement our analysis of TraCE-21ka with two proxy records that approximate global climate variability for the last two million years. We use temperature reconstructions from the EPICA Dome C ice core in Antarctica (*28*). Temperature reconstructions from Antarctic ice cores primarily track global greenhouse gas concentrations and therefore global temperature changes (*103*). We also use global average surface temperature (GAST) reconstructions from Snyder (*30*). This estimate of GAST is based on proxy-based sea surface temperature reconstructions (SST) that are scaled to surface temperatures with a value determined by examining SST-surface air temperature differences from the Paleoclimate Modelling Intercomparison Project (PMIP) model simulations. Comparisons between GAST reconstructions, EPICA Dome C, and greenhouse gasses demonstrate that both sets of proxy records used here well approximate global climate evolution

(*30*). Variations in ocean circulation emerge in EPICA Dome C oxygen isotopes (*104*) but as a second-order feature imposed on greenhouse gas-controlled temperature changes. The spectral continuum of temperature variability at EPICA Dome C and global surface air reconstructions were fit between 100^{-1}-$15{,}000^{-1}$ years^{-1} (*9*) and $2{,}000^{-1}$-$100{,}000^{-1}$ years^{-1} (*10*), respectively.

Benchmarking TraCE-21ka Simulated Climate Variability Against Temperature12k

We compared TraCE-21ka to the Temperature12k database (*105*), a global compilation of proxy temperature reconstructions that span the last 12,000 years. Though, several proxy reconstructions within Temperature12k extend well beyond the last 12,000 years. We first filtered the Temperature12k database to remove all pollen-based temperature estimates and then estimated the continuum of global temperature variability in the same framework defined in the *TraCE-21ka and Proxy Paleoclimate Estimates* and *Spectral Analyses* section. That is, we estimated power spectra for Temperature12k at a site level, and then averaged across sites to produce a globally averaged power spectrum. For TraCE-21ka, we performed the same procedure after spatiotemporally subsampling and low-pass filtering the temperature simulations. Six of the non-pollen temperature estimates in Temperature12k failed spectral analyses for various reasons (Table S3). No similar comparisons are made for precipitation due to the lack of an analogous database to Temperature12k. However, low-frequency precipitation variability in TraCE-21ka likely results from thermodynamic effects of temperature changes (Clausius-Clapeyron relationship) given the nearly identical power spectra presented in Figure 2.

We find that TraCE-21ka can accurately simulate the three key features of the temperature continuum: 1) a high β at low frequencies (climate regime), 2) a low β at high frequencies (weather regime), and 3) a breakpoint in the scaling relationship between spectral power and frequency (Figure S13). In the low frequency, climate, regime β for Temperature12k is 1.83 and TraCE-21ka simulates a β of 1.87. In the high frequency, weather, regime Temperature12k has a β of 0.54 while TraCE-21ka has a β of -0.25. The location of the break in the scaling relationship for Temperature12k is 376^{-1} years^{-1} and 498^{-1} years^{-1} for TraCE-21ka. These results demonstrate that TraCE-21ka performs well, despite the general struggle of climate models to accurately simulate temporal persistence in the high frequency, weather, regime. Much like other comparisons between empirical climate observations against climate models, TraCE-21ka poorly simulates temporal persistence in temperature variability (i.e. lower β in TraCE-21ka) in the high frequency regime (*48*). Despite this deficiency, TraCE-21ka captures the key features of the temperature continuum and is well-suited as a climate benchmark against which we can compare our globally averaged power spectra of vegetation turnover.

Estimating the Highest Frequency for Unbiased Estimates of β

In light of the limitations and biases of MTM for estimating β (*58*), we sought to estimate the highest frequency that produces unbiased estimates of β for each of our spatially averaged power spectra. We used the undegraded, annually resolved TraCE-21ka near-surface temperature time series, from the closest grid cell corresponding to each fossil pollen site, as a target signal with a known power spectrum. We then temporally degraded the TraCE-21ka near-surface temperature as outlined in the *TraCE-21ka and Proxy Paleoclimate Estimates* section and compared these

degraded power spectra to the target, annually resolved signal to estimate the highest frequency where estimates of β are unbiased by sedimentary processes.

In our analyses and prior work (*10*), annually resolved near-surface temperature estimates from TraCE-21ka produce a power spectrum where spectral power is evenly distributed in a high frequency band (> 831^{-1} $year^{-1}$ from Figure 2). At frequencies lower than this breakpoint, temperature variability increases with frequency (*10*) (Figure S16). This pattern holds when averaged across all fossil pollen sites (global estimate in Figure S16), the extra-tropics (extra-tropical estimate in Figure S16), and the tropics (tropical estimate in Figure S16). Built upon the expectation that sedimentary processes such as sediment mixing (*57*), and sampling resolution, can decrease spectral power at the highest frequencies and increase β (*58*), we use the even distribution of spectral power in the high frequency band of the undegraded TraCE-21ka temperature power spectrum as the metric to identify when estimates of β become biased by sedimentary processes. We find that high frequency spectral power decreases in the degraded TraCE-21ka power spectra and β increases in all spatial averages (Figure S16). However, the temporal characteristics of fossil pollen sites in each spatial average vary, leading to a spurious decrease in spectral power and an increase in β at the highest frequencies that varies across the spatial averages. The high latitudes are well represented in our fossil pollen compilation with several short, fossil pollen records with very high resolution (Figure S6). Therefore, in the degraded global and extra-tropical average power spectra of temperature, β in the high frequency regime is unbiased up to a frequency of 58^{-1} and 57^{-1} $years^{-1}$, respectively (Figure S16). Above this frequency, there is a spurious decrease in spectral power and an increase in β (Figure S16). In contrast, tropical fossil pollen sites in our compilation are less well temporally resolved than the extra-tropics, which decreases the frequency where a spurious decrease in spectral power and increase in β begins to 160^{-1} $years^{-1}$ (Figure S16). Therefore, we fit β to frequencies lower than 58^{-1}, 57^{-1}, and 160^{-1} $years^{-1}$, in all analyses for global, extra-tropical, and tropical power spectra, respectively.

Statistical Comparisons between Estimated Parameters from Spectral Analyses

We compared all estimated parameters (β, break location) from our ensembles of averaged power spectra for temperature, precipitation, and vegetation turnover using two-sided Fisher-Pitman permutation tests. A permutation test is used to determine whether the difference between two groups is statistically significant, without making assumptions about the underlying distribution of the data. In our analysis, we use permutation tests to compare the medians of the estimated parameters between different variables (e.g., temperature vs. vegetation turnover). The process works as follows:

1. We calculated the observed difference in medians between the two groups.
2. We then randomly reassigned the data points to the two groups and recalculated the difference in medians.
3. This process is repeated 10,000 times to create a distribution of possible differences under the null hypothesis of no true difference between groups.
4. We compare our observed difference to this distribution. If the observed difference falls in the 2.5% tails on either side, we consider the difference statistically significant at the 0.05 level.

This approach allows us to assess whether the observed differences in our spectral parameters are likely to have occurred by chance. We report the results of all these comparisons in Table S4 to Table S9.

We also test when estimated parameters are significantly different from 0 (and 2 for β) based on the confidence interval for the median parameter estimate across the ensemble for each parameter (Table S1). We calculated confidence intervals by bootstrapping the median. That is, each ensemble of parameter estimates was randomly resampled with replacement and the median was calculated for this random resample. This procedure was repeated 10,000 times to return a distribution of median estimates for each parameter. From this distribution of bootstrapped median estimates, we report the 2.5% and 97.5% percentiles as the 95% CI.

Methodological Constraints on Milankovitch Signal Detection

Milankovitch cycles are a primary control of global climate (*106*, *107*) and have been identified in fossil pollen records that span the last 2,000,000 years (*108*, *109*). Our analyses demonstrate increased spectral power associated with precession cycles at $21{,}000^{-1}$ $years^{-1}$ in all spatially averaged power spectra but high spectral power in the obliquity band ($41{,}000^{-1}$ $years^{-1}$) is missing and high spectral power in the eccentricity band ($100{,}000^{-1}$ $years^{-1}$) is only present in the vegetation turnover power spectrum for tropical sites (Figure 3). We find that these missing periodicities result from 1) our dimensionality reduction procedure (i.e. PCO), 2) the spatial scale of our compilation, 3) few sites that span enough time to resolve variability in the Milankovitch bands, and 4) variable temporal resolution of the data at each of these few sites.

Individual taxa or groups of taxa often demonstrate periodicity (as seen with arboreal pollen in (*108*) and (*109*)), but when all taxa are included in the dissimilarity matrix for PCO, as we do here, the periodicity becomes less pronounced. The Ioannina dataset demonstrates this well (Dataset ID: 4112) (*110*). Arboreal pollen at Ioannina has a strong cyclical pattern (*110*), but this is weakened when all taxa are included to create the dissimilarity matrix for PCO (Figure S15). The power spectrum at Ioannina does have somewhat higher spectral power in the Milankovitch bands but is lower than expected from the arboreal pollen abundance (Figure S15) (*110*). Variable phase response across taxa can also diminish the expression of periodic signals in the leading component (e.g., from PCO)

Furthermore, when averaging across a global compilation of sites with variable temporal data resolution, 41,000 and 100,000 year periodicities decrease in amplitude, even though individual sites demonstrate periodicity in these bands (e.g. ODP Site 658 (41194) and Páramo de Agua Blanca (21978) in Figure S15A). As site-level power spectra are averaged to form an estimate of the global power spectrum, high spectral power in the Milankovitch bands decreases even though it is present at individual sites (Figure S15B). We hypothesize that high spectral power at $21{,}000^{-1}$ $years^{-1}$ remains because we have more sites with a temporal span and sufficient data resolution that can resolve the 21,000 year periodicity, as compared to the 41,000 and 100,000 year periodicities (Table S2). The limited number of observations from high latitudes (> 65 °N), where obliquity effects are expected to be the dominant mode of variability (*111*), may also explain why we detect precession but not obliquity signals in our spatial distribution of sites. In

addition, precession has had a large influence on summer insolation over the last 400,000 years (*112*), which may also partly explain a clear precession signal and the absence of obliquity and eccentricity signals.

Uncertainty Estimation

We quantified uncertainty in our estimates of spectral power and the spectral continuum through Monte Carlo resampling of sites and Bchron posterior age estimates. Specifically, we drew 1,000 sites from our global compilation of 1,321 sites at random, and for each site, we drew a single posterior age estimate for MTM. We then downsampled TraCE-21ka accordingly, as described in the *TraCE-21ka and Proxy Paleoclimate Estimates* section, and then performed MTM as described in the *Spectral Analysis* section. We repeated this procedure 1,000 times, which produced an ensemble of 1,000 estimates of global spectral power, β, and breakpoint locations, for climate and fossil pollen turnover, from which we reported the median and 95% confidence interval (Figure S8, Figure S9, Table S1). All sampling was performed using a uniform distribution without replacement. This uncertainty estimation procedure assesses the influence of age model uncertainty and site selection on the global and latitudinally averaged power spectra.

Sensitivity Tests

We assessed the sensitivity of our results to our choice of fossil pollen dimensionality reduction and power spectra estimation methods (Figure S3, Figure S10, Figure S11, Figure S12). For dimensionality reduction, we tested alternative methods to reduce fossil pollen dimensionality and also tested various community dissimilarity metrics. In these sensitivity tests, we calculated community dissimilarity using the Bray Curtis and Jaccard dissimilarity metrics. We also performed correspondence analysis after square root transforming the fossil pollen assemblages, which, unlike PCO, does not assume linearity (*113*). Lastly, to test the sensitivity of our analyses to fossil pollen analytical accuracy, we degraded the percent abundance fossil pollen observations to presence/absence, though the Jaccard distance metric is presence/absence based as well.

Changing the dissimilarity metric and the dimension of variability analyzed had limited impacts on our conclusions, however, correspondence analyses produced results with the least total spectral power (Figure S3, Figure S10). We hypothesize that this occurs because PCO assumes linearity in the species-matrix decomposition while correspondence analysis does not assume linearity (*113*). Correspondence analysis also produced slightly different results for latitudinally averaged power spectra because of the scaling procedure we implemented (Figure S11, Figure S12). The eigenvalues in correspondence analyses do not indicate variance explained as they do in PCO. Rather, eigenvalues correspond to correlation coefficients between the coordinates for species in the fossil pollen assemblage (i.e. species score) and coordinates for time intervals (i.e. site score) in the ordination coordinate system. However, our scaling procedure, which assumes that the eigenvalues correspond to variance explained, is incompatible with correspondence analysis. Nevertheless, we include sensitivity tests for correspondence analysis to assess the assumption of linearity in PCO and the influence of metric saturation on our results. We chose to present the first dimension from PCO using the squared chord distance metric because of strong

support for the efficacy of the squared chord distance metric to discriminate fossil pollen assemblages that source from distinct ecosystems (*26*, *88*).

We also tested different methods for estimating the global spectral continuum of vegetation turnover by taking the mean of MTM adaptive spectral power (as shown in the main text), taking the median of MTM adaptive spectral power, averaging MTM spectral eigencoefficients, and averaging β for each site. The methodology for median estimates of MTM adaptive spectral power was identical to the main manuscript except we took the median, not the mean as in the main text. The procedure for returning a global average of spectral power by averaging eigencoefficients was nearly identical to averaging by spectral power. We first performed MTM on a single site and retained the five spectral eigencoefficients for each site that correspond to the five data tapers. We then averaged the five eigencoefficients across all sites by binning by frequency, as described in the *Spectral Analysis* section. We then calculated spectral power at each frequency using the averaged eigencoefficients and Equation 1, where $\hat{S}_k(f)$ is spectral power and $y_k(f)$ is the eigencoefficient for the kth data taper. Since we use five data tapers, this produces five estimates of $\hat{S}_k(f)$ which we average to estimate total spectral power (*22*).

$$\hat{S}_k(f) = |y_k(f)|^2 \quad \text{(Equation 1)}$$

These estimates of total spectral power were used to estimate β. The eigencoefficient averaging provides an important complementary view to the MTM adaptive spectral power approaches noted above, as it explicitly considers signal phase at each site. That is, strong signals that are antiphased at different locations will cancel, instead of being amplified as the case for the MTM adaptive spectral power approaches. Eigencoefficient averaging is expected to reduce the overall power at a given frequency in the reconstructed spectrum and to diminish periodic signals that are not in phase globally since it allows for destructive interference across sites.

Lastly, we estimated the global continuum of vegetation turnover by directly averaging β at each site. Here, we performed MTM at each site as described in the *Spectral Analysis* section and then estimated β using an ordinary least squares regression in log-log space, retaining β at each site, not spectral power. Estimates of β were then averaged across sites resulting in a global estimate of the spectral continuum of fossil pollen turnover. These sensitivity tests were performed within the same Monte Carlo framework that we use to quantify uncertainty for the fossil pollen assemblages and TraCE-21ka climate parameters.

Our conclusions are robust to the method used to aggregate individual site-level power spectra of vegetation turnover into a global estimate. All three approaches reveal four characteristic timescales in global vegetation turnover each with distinct βs: high β at the highest frequencies, low β in the high-intermediate frequency band, high β in the low-intermediate frequency band, and low β in the low frequency band (Figure S3). Across much of the frequency space, uncertainties for these approaches overlap, particularly at high and low frequencies where spectral power estimates diverge.

This divergence is most prominent in two areas: the high and low frequencies. At low frequencies, global estimates that use the mean of site-level power spectra have greater spectral power than estimates that use the median of site-level power spectra and the mean of site-level

eigencoefficient estimates (Figure S3). At high frequencies, global estimates that use the median of site-level power spectra and the mean of site-level eigencoefficient estimates have a band-limited increase in the globally estimated spectral power, not present when in the global estimate that uses the mean of site-level power spectra (Figure S3). These discrepancies may stem from the different underlying distributions of site-level spectral power and eigencoefficient estimates, and the phase relationships that are preserved in the eigencoefficient estimates.

The spectral power estimates from MTM of a Gaussian process follow a chi-square distribution with two degrees of freedom, while the distribution of eigencoefficients approximately follows a normal distribution (*22*, *114*). This suggests that the estimated global power spectra of vegetation turnover using the mean of site-level spectral power should be systematically higher than median estimates and mean of eigencoefficient estimates, while the latter two should be similar. Our sensitivity tests capture this systematic offset (Figure S3) and explain higher spectral power at low frequencies when using the mean of site-level spectral power. At low frequencies, individual sites with high spectral power pull the global estimate to higher values. While this offset should also exist at high frequencies, we observe a counterintuitive result: individual sites with low spectral power pull the global estimate that uses the mean of site-level spectral power lower than the median and eigencoefficient global estimates (Figure S3). In light of this unexpected observation, and considering that each approach produces identical conclusions, we present results using the mean of spectral power to maintain consistency with prior studies (*9*, *10*, *23*).

In contrast to the robust conclusions when estimating the globally averaged power spectra of vegetation turnover using the mean, median, and mean of eigencoefficients we find that results were highly sensitive to averaging by β. This is a product of our piecewise regression procedure to determine the location of breaks in the log-log fit between spectral power and frequency in the high and intermediate frequency bands. Accurately identifying the location of breaks in β between the high and high-intermediate frequency bands requires high-resolution sampling which is present in a subset of fossil pollen assemblages (Figure S3, Figure S10). Performing breakpoint identification on spectral power at a site level increases the weight of the more abundant lower-resolution sites and reduces the weight of the less abundant high-resolution sites, reducing frequency resolution and biasing estimates of globally averaged β.

Lastly, we assessed the sensitivity of our conclusions to the influence of anthropogenic land-use change. We performed all analyses after first removing any samples from the last 2,000 years (*56*), when anthropogenic influences in fossil pollen records are strongly expressed (*61*). Removing any samples within the last 2,000 years produces nearly identical power spectra at frequencies lower than 100^{-1} $years^{-1}$ and suggests that climate tracking at millennial to multi-centennial scales persists (Figure 2, Figure S14). However, the detected breakpoints and β change if samples from the last 2,000 years are removed. The high frequency breakpoint (Figure 2, 146^{-1} $years^{-1}$) decreases to 539^{-1} $years^{-1}$ and β decreases from 4.58 to 0.39; the breakpoint at 759^{-1} $years^{-1}$ decreases to $3{,}673^{-1}$ $years^{-1}$ and β increases from -0.1 to 2.02; the breakpoint at $17{,}505^{-1}$ $years^{-1}$ decreases to $21{,}717^{-1}$ $years^{-1}$ and β decreases from 1.84 to 0.90; and β for the lowest frequencies increases from -0.28 to 0.09. Our sampling density increases as age decreases (Figure S6) and sites with the highest temporal resolution span the last 2,000 years (Table S2), therefore these changes in breakpoints and β may be a result of reduced sampling density. Despite statistically different βs at the highest frequencies, globally averaged power spectra still

demonstrate a decrease in spectral power in the high frequency band which is particularly well demonstrated in the confidence intervals, matching results from the main manuscript (Figure 2, Figure S14) and results from similar analyses at a continental scale that also remove fossil pollen observations from the last 2,000 years (*56*). This suggests that climate decoupling at the highest frequencies may contain some influence of anthropogenic land use change (*62*, *115*) but this is not the only control on high frequency vegetation turnover.

Supplemental Tables and Figures

Vegetation

	β						Breakpoint
	High Frequency Band	High-Intermediate Frequency Band	Low-Intermediate Frequency Band	Low Frequency Band	High Frequency Band - High-Intermediate Frequency Band ($^{-1}$ years^{-1})	High-Intermediate Frequency Band - Low-Intermediate Frequency Band ($^{-1}$ years^{-1})	Low-Intermediate Frequency Band – Low Frequency Band ($^{-1}$ years^{-1})
Global	4.58*† (4.02, 5.12)	-0.10† (-0.21, 0.09)	1.84*† (1.76, 1.90)	-0.28*† (-0.47, -0.10)	146* (150, 141)	759* (802, 768)	17,505* (18,162, 16,831)
Extra-tropics (> 23.5°)	4.51*† (3.99, 4.96)	-0.46*† (-0.54, -0.38)	2.21*† (2.17, 2.26)	-0.15† (-0.35, 0.07)	143* (148, 140)	696* (722, 680)	14,289* (15,017, 13,797)
Tropics (< 23.5°)	1.20*† (1.14, 1.29)			-0.50*† (-0.55, -0.43)			7,609* (7,921, 6,997)

TraCE-21ka near-surface Temperature (2 m)

	β	Breakpoint

	High Frequency Band (Weather Regime)	Low Frequency Band (Climate Regime)	High Frequency Band - Low Frequency Band. ($^{-1}$ years^{-1})
Global	-0.28*† (-0.33, -0.21)	3.11*† (3.08, 3.14)	664* (689, 645)
Extra-tropics (> 23.5°)	-0.29*† (-0.34, -0.24)	3.15*† (3.12, 3.19)	665* (668, 647)
Tropics (< 23.5°)	0.99*† (0.95, 1.03)	3.08*† (3.06, 3.11)	910* (922, 890)

1405

TraCE-21ka Annual Precipitation Rate

B **Breakpoint**

	High Frequency Band (Weather Regime)	Low Frequency Band (Climate Regime)	High Frequency Band - Low Frequency Band ($^{-1}$ years^{-1})
Global	-0.52*† (-0.59, -0.47)	2.69*† (2.68, 2.71)	675* (691, 663)
Extra-tropics (> 23.5°)	-0.99*† (-1.03, -0.95)	2.52*† (2.51, 2.43)	629* (633, 620)
Tropics (< 23.5°)	0.49*† (0.40, 0.61)	2.46*† (2.45, 2.49)	807* (829, 779)

1406 **Table S1.** Parameter estimates and corresponding 95% confidence intervals (in parentheses) for
1407 Figures 2 and 3. * indicates that the estimated parameter is statistically distinct from 0 based on
1408 the bootstrapped confidence interval. For estimates of β, † indicates that β is statistically distinct
1409 from 2 (i.e. red noise) based on the bootstrapped confidence interval (for methods, see section
1410 *Statistical Comparisons between Estimated Parameters from Spectral Analyses*).
1411
1412 **Table S2.** (Not within the Supplementary text but available as a Supplementary File) The list of
1413 sites considered in this study including those that were filtered out for issues with taxonomy
1414 harmonization, data quality (negative abundances), or chronological controls that prevented
1415 developing age models.
1416

Site Name	Dataset ID	Failure Reason
Challa Lake	hXPNKEOsFdftFMmUvYYv	No age information in Temperature12k
Lake Malawi	Ff4CF5LsHToo394MMeFt	Not enough RAM for linterpLH13 interpolation algorithm

Midden Cluster 3	yCebthVVgiBnTTu63yvd	No resolvable frequencies determined by linterpLH13 interpolation algorithm
Midden Cluster 5	Mq5F6F6nmLYKNlACGome	No resolvable frequencies determined by linterpLH13 interpolation algorithm
Middel Cluster 6	39OKoIAcvAICa26B8Oiy	No resolvable frequencies determined by linterpLH13 interpolation algorithm
Soylegrotta	Ipsz1iUTCMtvZqRnxzs8	No resolvable frequencies determined by linterpLH13 interpolation algorithm

Table S3. Temperature12k sites that failed spectral analyses and the corresponding reason.

	Vegetation Turnover β High Frequency Band	Vegetation Turnover β High-Intermediate Frequency Band	Vegetation Turnover β Low-Intermediate Frequency Band	Vegetation Turnover β Low Frequency Band	TraCE-21ka Temperature β High Frequency Band	TraCE-21ka Temperature β Low Frequency Band	TraCE-21ka Annual Precipitation Rate β High Frequency Band	TraCE-21ka Annual Precipitation Rate β Low Frequency Band
Vegetation Turnover β High Frequency Band								
Vegetation Turnover β High-Intermediate Frequency Band	< 0.001***							
Vegetation Turnover β Low-Intermediate Frequency Band	< 0.001***	< 0.001***						
Vegetation Turnover β Low Frequency Band	< 0.001***	0.0543	< 0.001***					
TraCE-21ka Temperature β High Frequency Band	< 0.001***	0.0069**	< 0.001***	0.882				
TraCE-21ka Temperature β Low Frequency Band	< 0.001***	< 0.001***	< 0.001***	< 0.001***	< 0.001***			
TraCE-21ka Annual Precipitation	< 0.001***	< 0.001***	< 0.001***	0.33	< 0.001***	< 0.001***		

Rate β High Frequency Band								
TraCE-21ka Annual Precipitation Rate β Low Frequency Band	< 0.001***	< 0.001***	< 0.001***	< 0.001**	< 0.001***	< 0.001***	< 0.001***	

Table S4. P-values of permutation tests comparing β from Figure 2 where *** corresponds to values <0.001, ** indicates values between 0.001 and 0.01, and * indicates values between 0.01 and 0.05.

	Vegetation Turnover High Frequency Band - High-Intermediate Frequency Band Break Location	Vegetation Turnover High-Intermediate Frequency Band - Low-Intermediate Frequency Band Break Location	Vegetation Turnover Low-Intermediate Frequency Band - Low Frequency Band Break Location	TraCE-21ka Temperature High Frequency Band - Low Frequency Band Break Location	TraCE-21ka Annual Precipitation Rate High Frequency Band - Low Frequency Band Break Location
Vegetation Turnover High Frequency Band - High-Intermediate Frequency Band Break Location					
Vegetation Turnover High-Intermediate Frequency Band - Low-Intermediate Frequency Band Break Location	< 0.001***				
Vegetation Turnover Low-Intermediate Frequency Band - Low Frequency Band Break Location	< 0.001***	< 0.001***			
TraCE-21ka Temperature High Frequency Band - Low Frequency Band Break Location	< 0.001***	0.0083**	< 0.001***		
TraCE-21ka Annual Precipitation Rate High Frequency Band - Low Frequency Band Break Location	< 0.001***	< 0.001***	< 0.001***	0.323	

Table S5. P-values of permutation tests comparing break locations from Figure 2 where *** corresponds to values <0.001, ** indicates values between 0.001 and 0.01, and * indicates values between 0.01 and 0.05.

Latitude > 23.5°	Latitude > 23.5°	Latitude > 23.5°	Latitude > 23.5°	Latitude > 23.5°	Latitude > 23.5°	Latitude > 23.5°	Latitude > 23.5°

	Vegetation Turnover β High Frequency Band	Vegetation Turnover β High-Intermediate Frequency Band	Vegetation Turnover β Low-Intermediate Frequency Band	Vegetation Turnover β Low Frequency Band	TraCE-21ka Temperature β High Frequency Band	TraCE-21ka Temperature β Low Frequency Band	TraCE-21ka Annual Precipitation Rate β High Frequency Band	TraCE-21ka Annual Precipitation Rate β Low Frequency Band
Latitude > 23.5° Vegetation Turnover β High Frequency Band								
Latitude > 23.5° Vegetation Turnover β High-Intermediate Frequency Band	< 0.001***							
Latitude > 23.5° Vegetation Turnover β Low-Intermediate Frequency Band	< 0.001***	< 0.001***						
Latitude > 23.5° Vegetation Turnover β Low Frequency Band	< 0.001***	0.0224*	< 0.001***					
Latitude > 23.5° TraCE-21ka Temperature β High Frequency Band	< 0.001***	< 0.001***	< 0.001***	0.0224*				
Latitude > 23.5° TraCE-21ka Temperature β Low Frequency Band	< 0.001***	< 0.001***	< 0.001***	< 0.001***	< 0.001***			
Latitude > 23.5° TraCE-21ka Annual Precipitation Rate β High	< 0.001***	< 0.001***	< 0.001***	< 0.001***	< 0.001***	< 0.001***		

Frequency Band								
Latitude > 23.5° TraCE-21ka Annual Precipitation Rate β Low Frequency Band	< 0.001***	< 0.001***	< 0.001***	< 0.001***	< 0.001***	< 0.001***	< 0.001***	

Table S6. P-values of permutation tests comparing β for the extra-tropics from Figure 3 where *** corresponds to values <0.001, ** indicates values between 0.001 and 0.01, and * indicates values between 0.01 and 0.05.

	Latitude > 23.5° Vegetation Turnover High Frequency Band - High-Intermediate Frequency Band Break Location	Latitude > 23.5° Vegetation Turnover High-Intermediate Frequency Band - Low-Intermediate Frequency Band Break Location	Latitude > 23.5° Vegetation Turnover Low-Intermediate Frequency Band - Low Frequency Band Break Location	Latitude > 23.5° TraCE-21ka Temperature High Frequency Band - Low Frequency Band Break Location	Latitude > 23.5° TraCE-21ka Annual Precipitation Rate High Frequency Band - Low Frequency Band Break Location
Latitude > 23.5° Vegetation Turnover High Frequency Band - High-Intermediate Frequency Band Break Location					
Latitude > 23.5° Vegetation Turnover High-Intermediate Frequency Band - Low-Intermediate Frequency Band Break Location	< 0.001***				
Latitude > 23.5° Vegetation Turnover Low-Intermediate Frequency Band - Low Frequency Band Break Location	< 0.001***	< 0.001***			
Latitude > 23.5° TraCE-21ka Temperature High Frequency Band - Low Frequency Band Break Location	< 0.001***	0.0109*	< 0.001***		
Latitude > 23.5° TraCE-21ka Annual Precipitation Rate High Frequency Band - Low Frequency Band Break Location	< 0.001***	< 0.001***	< 0.001***	< 0.001***	

Table S7. P-values of permutation tests comparing break locations for the extra-tropics from Figure 3 where *** corresponds to values <0.001, ** indicates values between 0.001 and 0.01, and * indicates values between 0.01 and 0.05.

	Latitude < 23.5° Vegetation Turnover High Frequency Band – Low Frequency Band Break Location	Latitude < 23.5° TraCE-21ka Temperature High Frequency Band - Low Frequency Band Break Location	Latitude < 23.5° TraCE-21ka Annual Precipitation Rate High Frequency Band - Low Frequency Band Break Location
Latitude < 23.5° Vegetation Turnover High Frequency Band – Low Frequency Band Break Location			
Latitude < 23.5° TraCE-21ka Temperature High Frequency Band - Low Frequency Band Break Location	< 0.001***		
Latitude < 23.5° TraCE-21ka Annual Precipitation Rate High Frequency Band - Low Frequency Band Break Location	< 0.001***	< 0.001***	

Table S8. P-values of permutation tests comparing break locations for the tropics from Figure 3 where *** corresponds to values <0.001, ** indicates values between 0.001 and 0.01, and * indicates values between 0.01 and 0.05.

	Latitude < 23.5° Vegetation Turnover β High Frequency Band	Latitude < 23.5° Vegetation Turnover β Low Frequency Band	Latitude < 23.5° TraCE-21ka Temperature β High Frequency Band	Latitude < 23.5° TraCE-21ka Temperature β Low Frequency Band	Latitude < 23.5° TraCE-21ka Annual Precipitation Rate β High Frequency Band	Latitude < 23.5° TraCE-21ka Annual Precipitation Rate β Low Frequency Band
Latitude < 23.5° Vegetation Turnover β High Frequency Band						
Latitude < 23.5° Vegetation Turnover β Low Frequency Band	< 0.001***					
Latitude < 23.5° TraCE-21ka	< 0.001***	< 0.001***				

Temperature β High Frequency Band						
Latitude < 23.5° TraCE-21ka Temperature β Low Frequency Band	< 0.001***	< 0.001***	< 0.001***			
Latitude < 23.5° TraCE-21ka Annual Precipitation Rate β High Frequency Band	< 0.001***	< 0.001***	< 0.001***	< 0.001***		
Latitude < 23.5° TraCE-21ka Annual Precipitation Rate β Low Frequency Band	< 0.001***	< 0.001***	< 0.001***	< 0.001***	< 0.001***	

Table S9. P-values of permutation tests comparing β for the tropics from Figure 3 where *** corresponds to values <0.001, ** indicates values between 0.001 and 0.01, and * indicates values between 0.01 and 0.05.

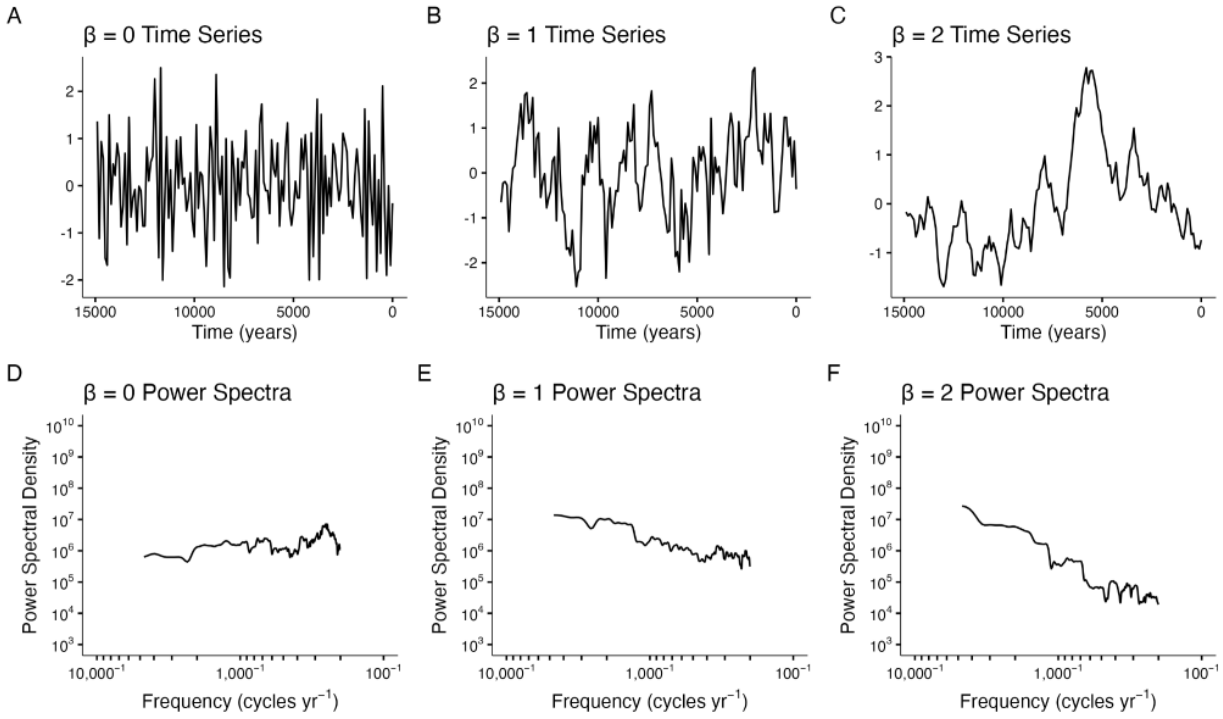

Figure S1. (A-C) Synthetic time series with arbitrary units with a β of (A) 0, (B) 1, and (C) 2. (D-F) The corresponding power spectra for the synthetic time series in (A-C).

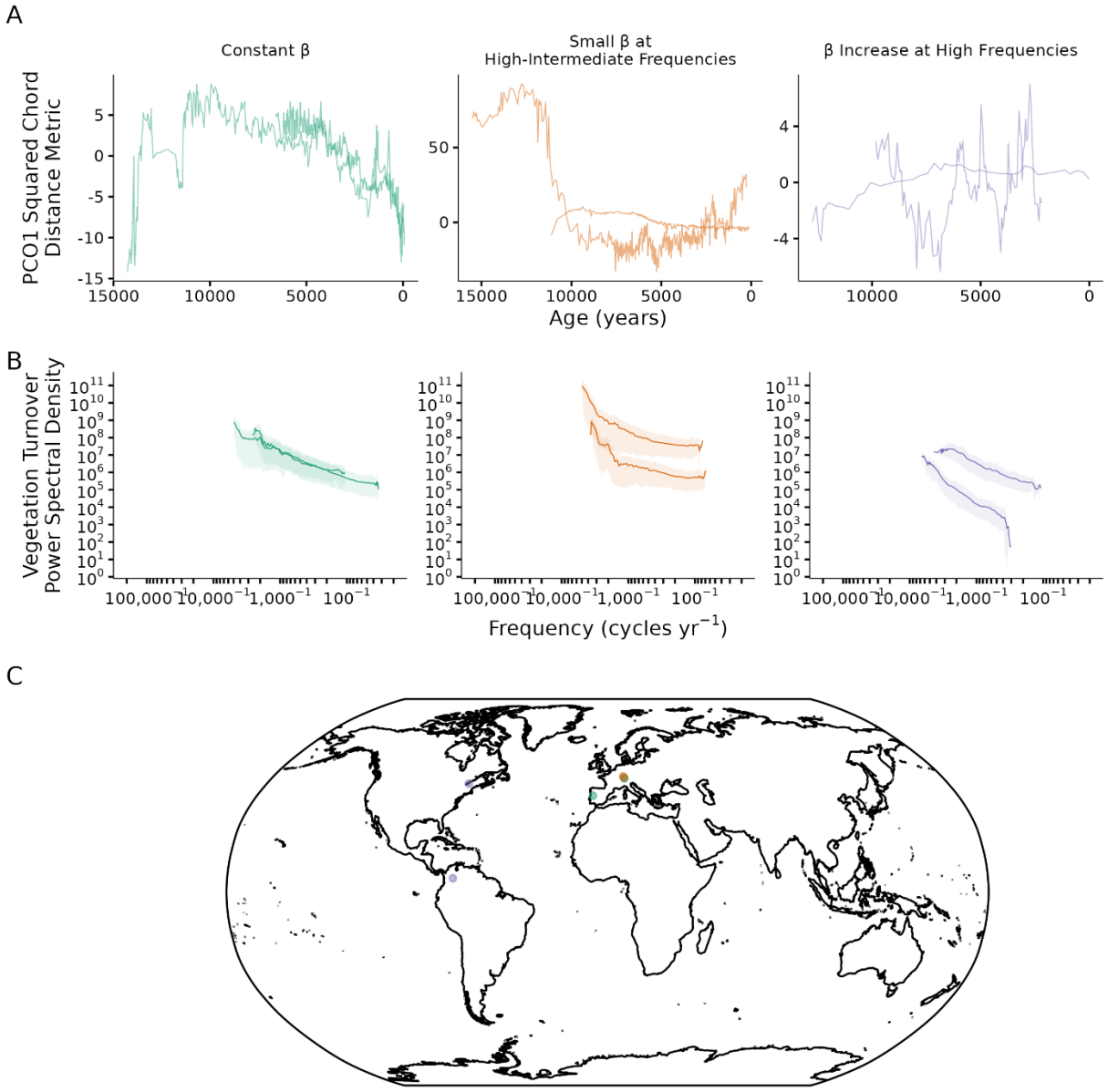

Figure S2. (A) Individual records of vegetation turnover from fossil pollen from the 1,321 site compilation that are selected to demonstrate characteristics of the global average power spectra that are presented in Figures 2 and 3. (B) The corresponding power spectra for the selected sites in (A). (C) A map of selected sites in (A-B). The colors correspond to different spectral characteristics that are highlighted in the main text. Green corresponds to sites that demonstrate a constant power-law scaling relationship across all frequencies and fast tracking at intermediate frequencies in the global average. Orange corresponds to sites that demonstrate a break in spectral power at low-intermediate frequencies (~1,000 years^{-1}) and a small β at high-intermediate frequencies. Purple indicates sites that demonstrate an increase in β at the highest frequencies. Note, that all sites demonstrate a decrease in β at multimillennial timescales present in the global average. Note, in (A) the PCO1 time series are scaled by the corresponding eigenvalue, unlike in Figure S7.

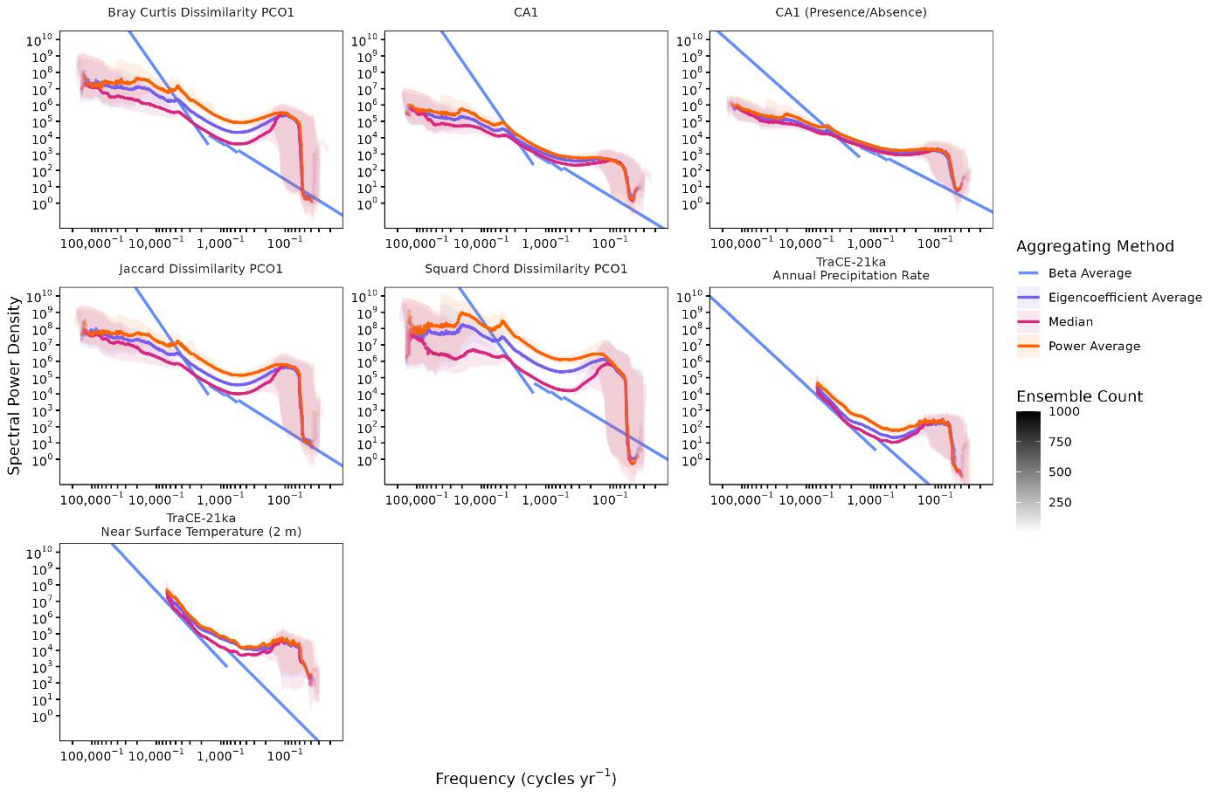

Figure S3. Sensitivity tests for the continuum of ecological variability, in which the dimensionality-reduction methods and spectral-averaging methods are varied. Power spectra line opacity indicates the number of ensemble members that resolve each frequency. Results are presented for the primary dimension of variability from dimensionality reduction on fossil pollen assemblages. For the power average approach, we bin by frequency and then average the spectral power values across sites. For the eigencoefficient average approach, we bin by frequency and average the five MTM eigencoefficients corresponding to each data taper. We calculate spectral power following Equation 1. For the β average approach, we estimate β through an ordinary least squares regression between spectral power and frequency at a single site. We then average across sites to produce a global estimate of β. This procedure only retains β, not spectral power. Therefore, for the β average method only the resulting β fit is presented. The separate lines for β average correspond to β in four frequency bands. The breakpoint of these two lines indicates the calculated average break location averaged across sites. All sensitivity analyses were performed with the Monte Carlo resampling procedure detailed in *Uncertainty Estimation* with the shaded area corresponding to the 95% confidence interval. Note, that all averaged power spectra based on PCO1 (the first axis of Principal Coordinates Analysis) of the site-level community dissimilarity matrix demonstrate a decrease in β after the common ~17,000^{-1} years^{-1} breakpoint (β = 0.45 for Bray-Curtis PCO1, β = 0.67 for Bray-Curtis PCO1, β = -0.28 for Squared Chord PCO1). This decrease is greatest in the squared chord dissimilarity metric which outperforms all other metrics for distinguishing modern fossil pollen assemblages that source from different ecosystems (i.e. is the most sensitive dissimilarity metric) (*26*, *88*). In contrast, CA1 (the first axis of Correspondence Analysis), which cannot saturate like metric-based approaches, shows no such decrease in β. The averaged power spectra for CA1, which represents the primary dimension of variation in fossil pollen assemblages (not the dissimilarity matrix), has a higher β

($\beta = 0.83$ for frequencies lower than the $17{,}824^{-1}$ years^{-1} breakpoint) and more consistent βs across all frequencies, demonstrating that the decrease in β observed at low frequencies for PCO-based approaches is caused by metric saturation.

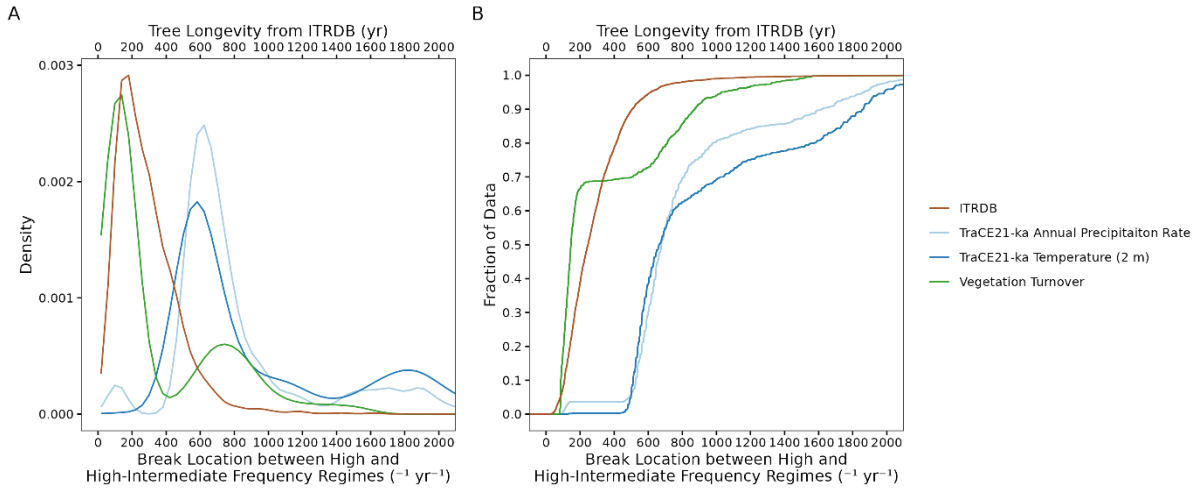

Figure S4. (A) Probability density distributions and (B) empirical cumulative distributions for the ensemble of breakpoint estimated for globally averaged power spectra between the low-intermediate and high-intermediate frequency band for fossil pollen (green) from our Monte Carlo resampling approach compared to tree longevity estimates from the International Tree Ring Data Bank (brown). Break locations for TraCE-21ka near-surface temperature (blue) and TraCE-21ka precipitation (light blue) correspond to one break location, previously reported (*9*, *10*), at frequencies between 100^{-1} to 1,000 years^{-1}. Tree longevity from the International Tree Ring Data Bank corresponds to the top horizontal axis. All pollen results presented are from PCO1 using the squared chord distance metric and averaged by spectral power.

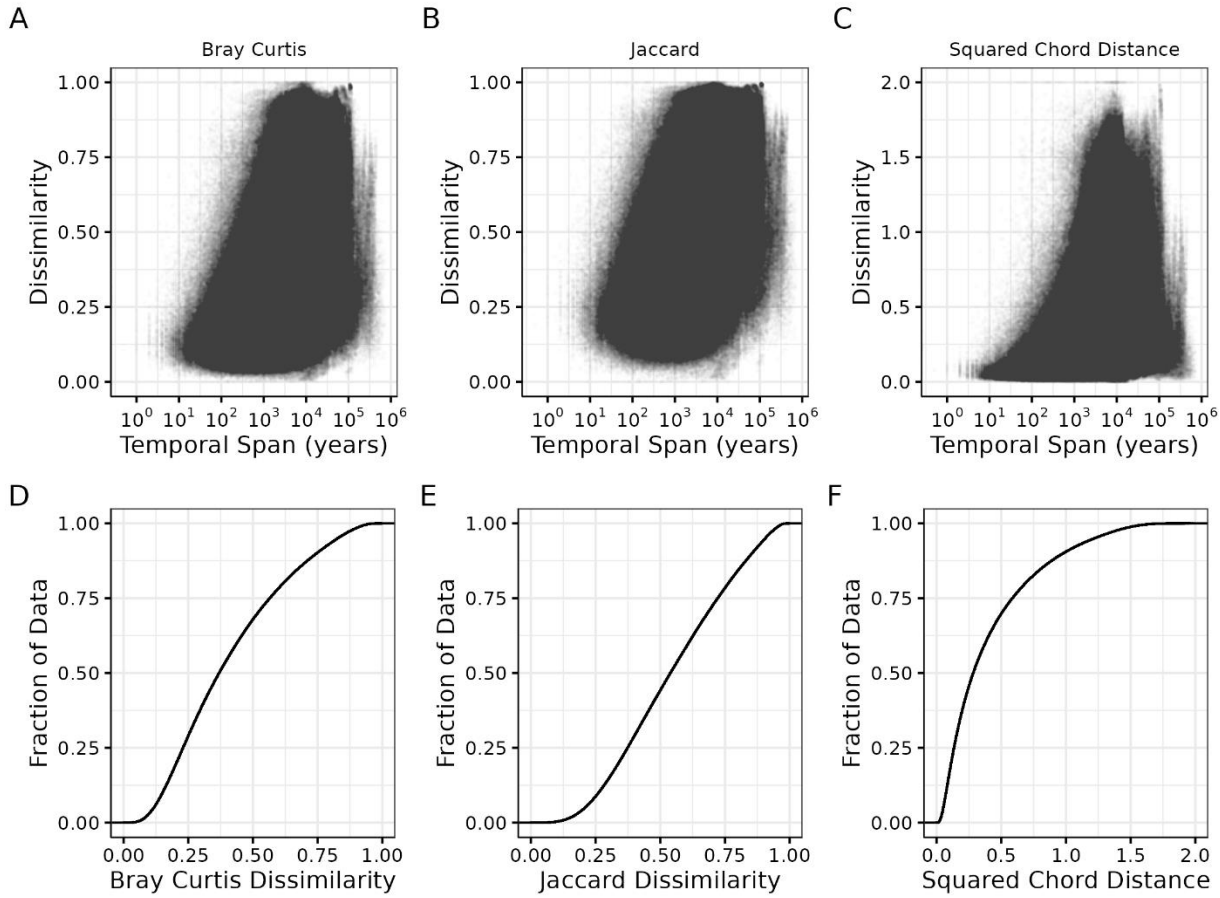

Figure S5. (A-C) Measured vegetation assemblage dissimilarity, for all sites in the global fossil pollen compilation. Dissimilarity was calculated only for assemblages from the same site and was not calculated for assemblages from different sites. Within each site, all possible pairs of fossil pollen assemblages were compared using the (A) Bray Curtis, (B) Jaccard, and (C) Squared Chord Distance metrics with the corresponding temporal span between the samples being compared retained. (D-F) The empirical cumulative distribution of all points shown in the top row of plots.

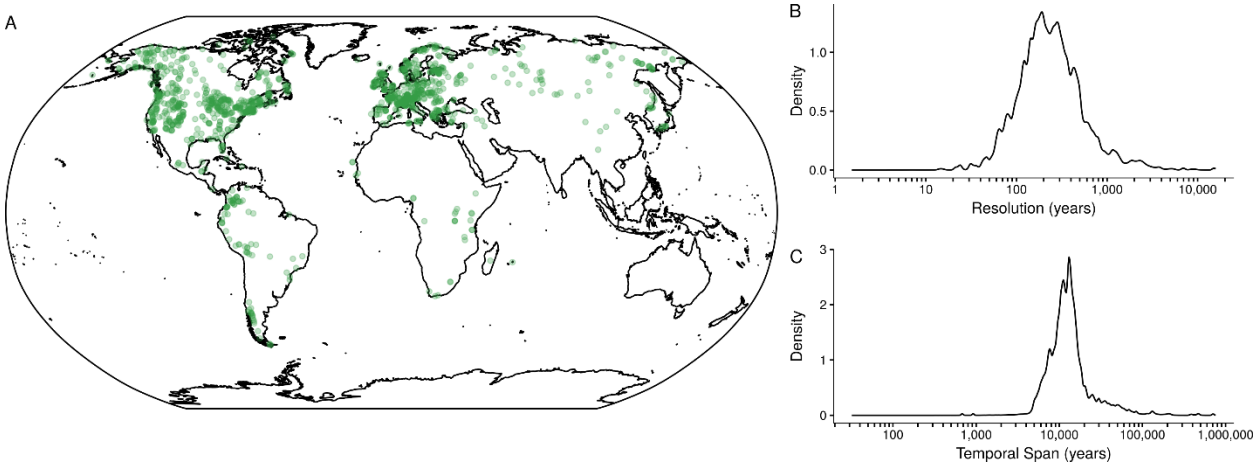

Figure S6. (A) All sites used in the spectral analyses, as in Figure 2A. The probability density of (B) temporal resolution and (C) temporal span for all sites analyzed and all corresponding posterior age estimates. Note, that the Northern Hemisphere is more well-represented than the Southern Hemisphere.

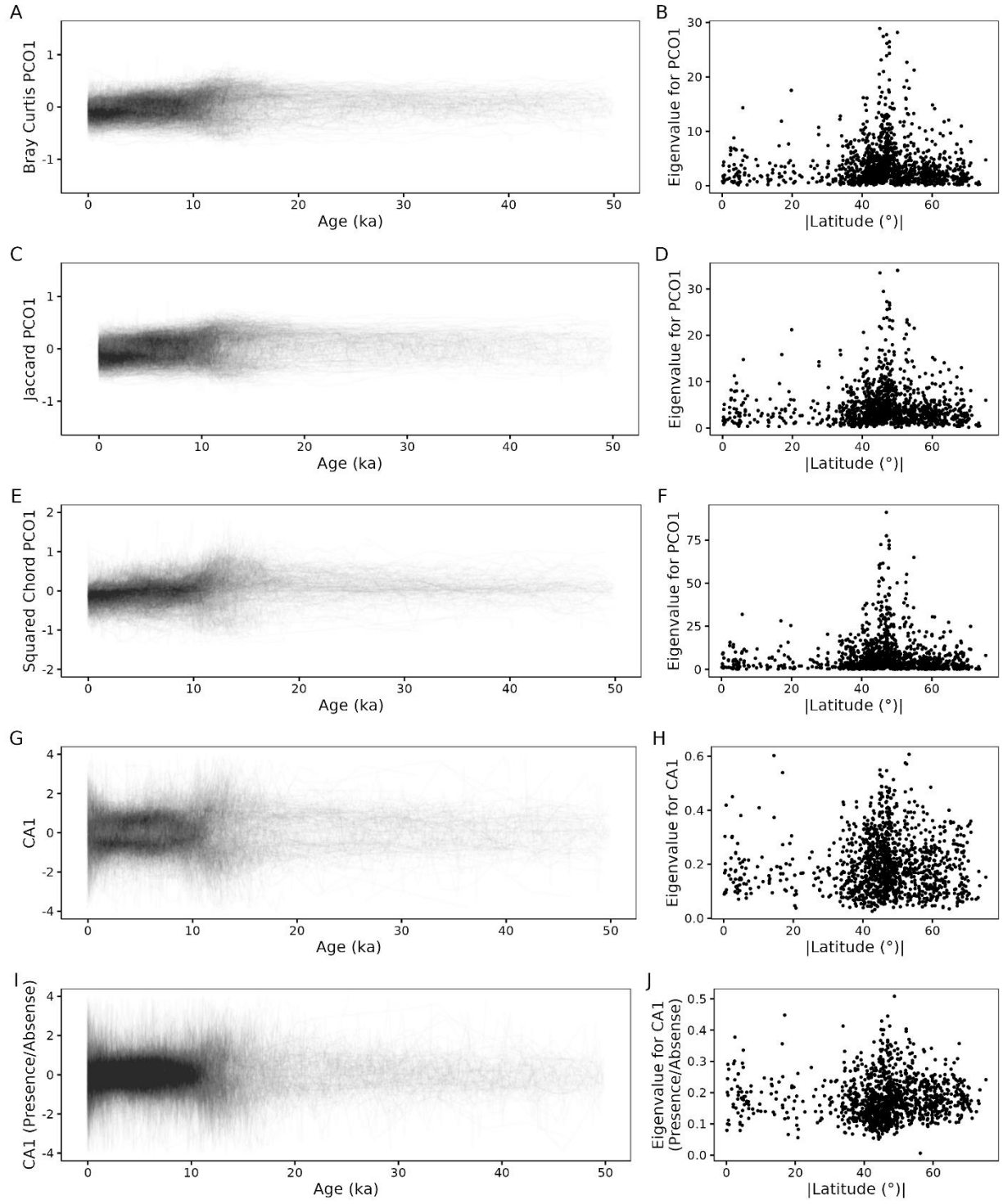

Figure S7. (A, C, E, G, I) The primary dimension of variability from 1) principal coordinates analyses (PCO) using the (A) Bray-Curtis, (C) Jaccard, and (E) Squared Chord Distance metrics

and 2) (G) correspondence analysis on fossil pollen assemblages for each site analyzed. We also performed correspondence analyses on fossil pollen assemblages after degrading the abundance observations to presence/absence (I). (B, D, F, H, J) Eigenvalues corresponding to PCO1 for each site plotted against the absolute value of the site latitude. For correspondence analyses, eigenvalues do not correspond to variance explained as they do for principal coordinate analyses. Rather, eigenvalues correspond to correlation coefficients between the coordinates for species in the fossil pollen assemblage (i.e. species score) and coordinates for time intervals (i.e. site score) in the ordination coordinate system. For visual simplicity, the PCO1 and CA1 results for each site are unscaled by the corresponding eigenvalue. Several scaled time series are presented in Figure S2. In addition, the right column (B, D, F, H, J) demonstrates that eigenvalues tend to be higher in the high latitudes, causing PCO1 for high-latitude sites to be upscaled, producing greater total spectral power in Figure 3, relative to the low latitudes. Also for visual simplicity, we only present sites here that span the last 50,000 years, we direct readers to our Zenodo repository (*74*) where all data are present.

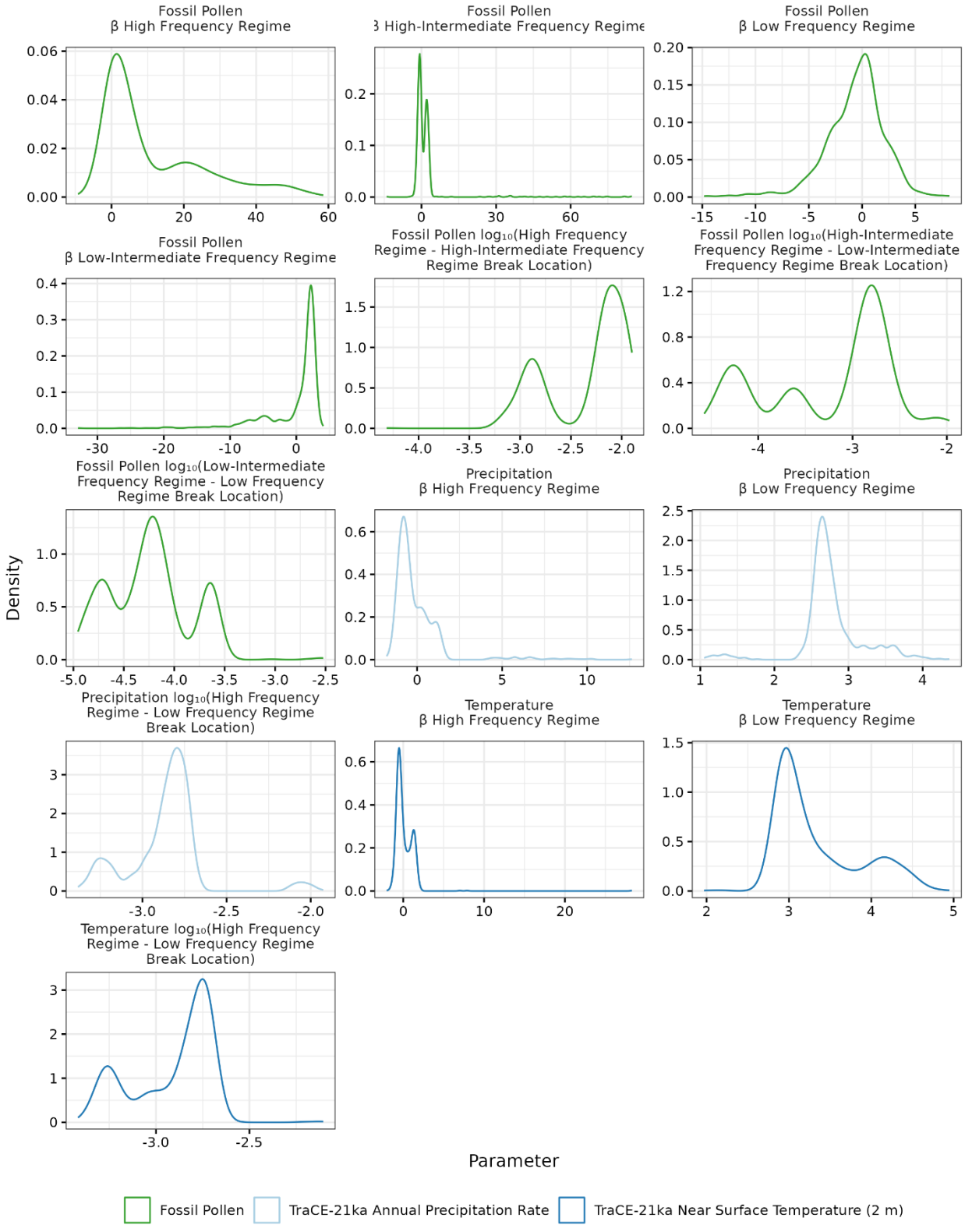

Figure S8. Each plot corresponds to the probability density function for all breakpoint and β parameter estimates in Figure 2 and Table S1. Colors correspond to parameter estimates for

fossil pollen (green), TraCE-21ka annual precipitation rate (light blue), and TraCE-21ka near-surface temperature (blue).

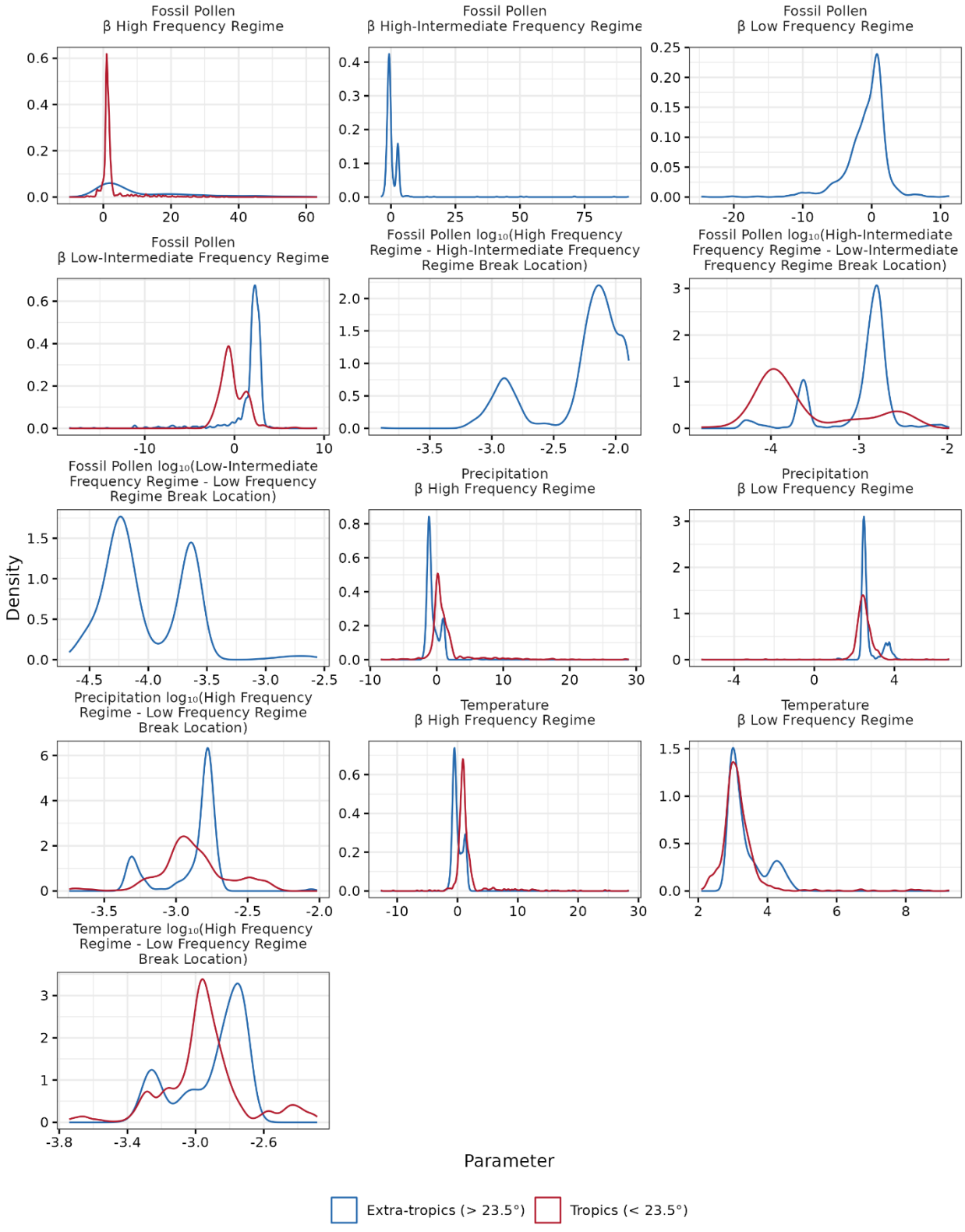

Figure S9. As in Figure S8 but for breakpoint and β estimates in Figure 3. Colors correspond to the spatial average with red indicating the tropics (< 23.5°) and blue indicating the extra-tropics (> 23.5°).

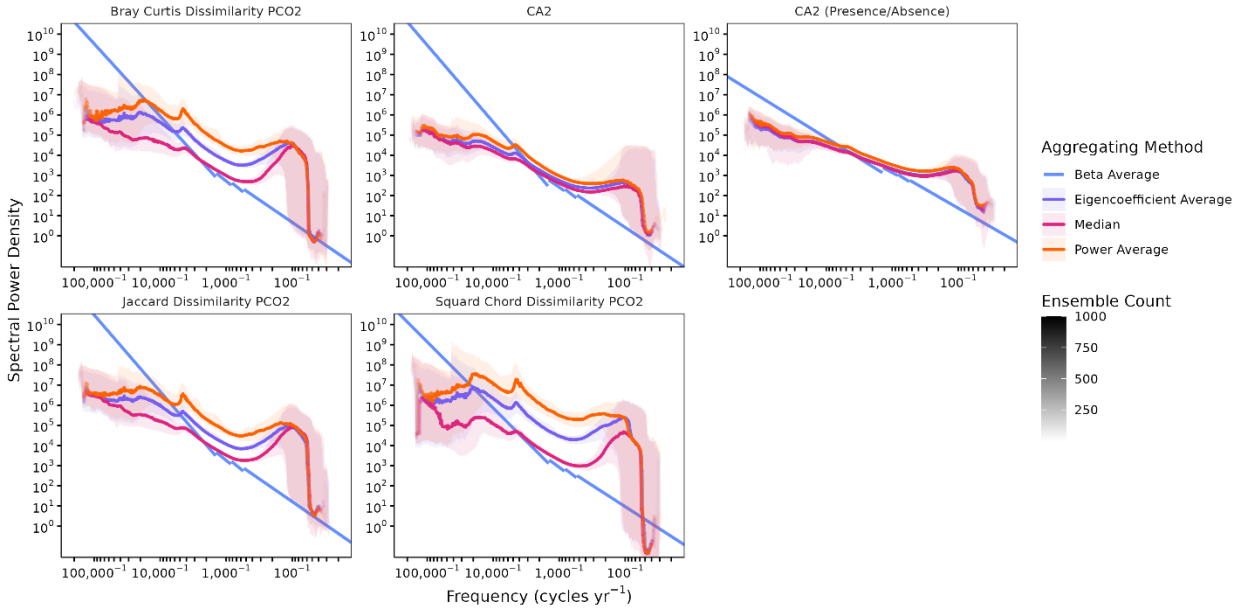

Figure S10. As in Figure S3 but for the secondary dimension of variability from dimensionality reduction on fossil pollen assemblages.

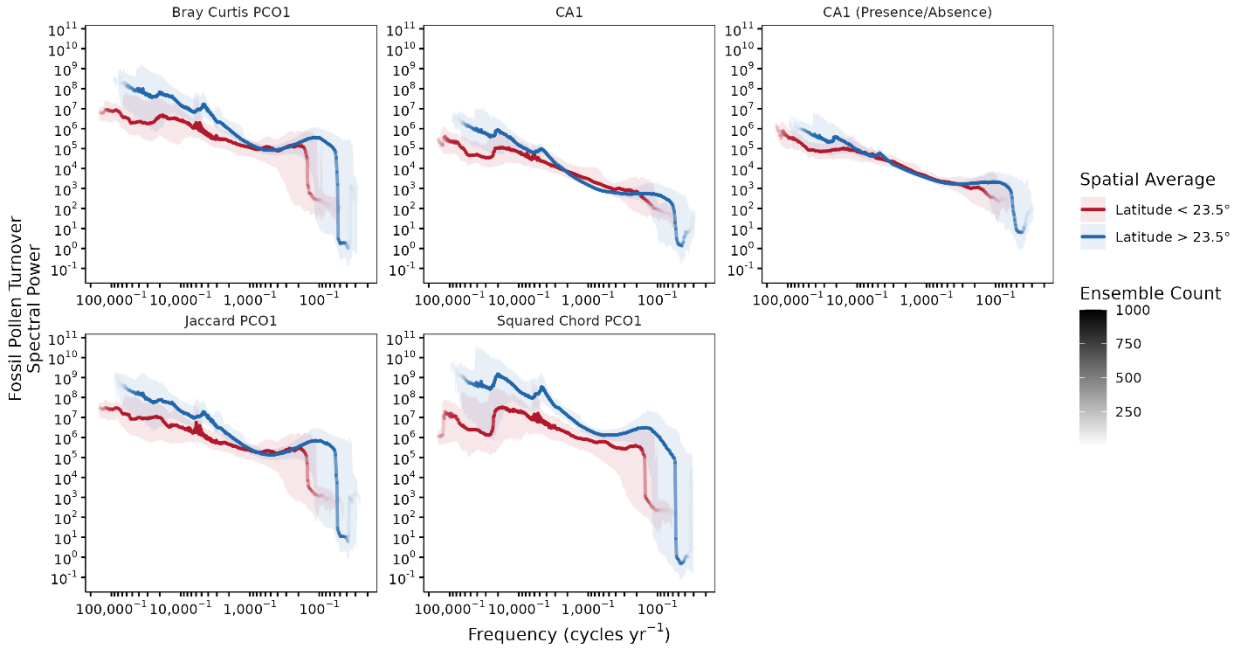

Figure S11. Sensitivity tests for latitudinal averaged power spectra for PCO1 of fossil pollen assemblages where the dimensionality reduction method is varied. All power spectra were generated by averaging spectral power after binning by frequency. Power spectra line opacity indicates the number of ensemble members that resolve each frequency.

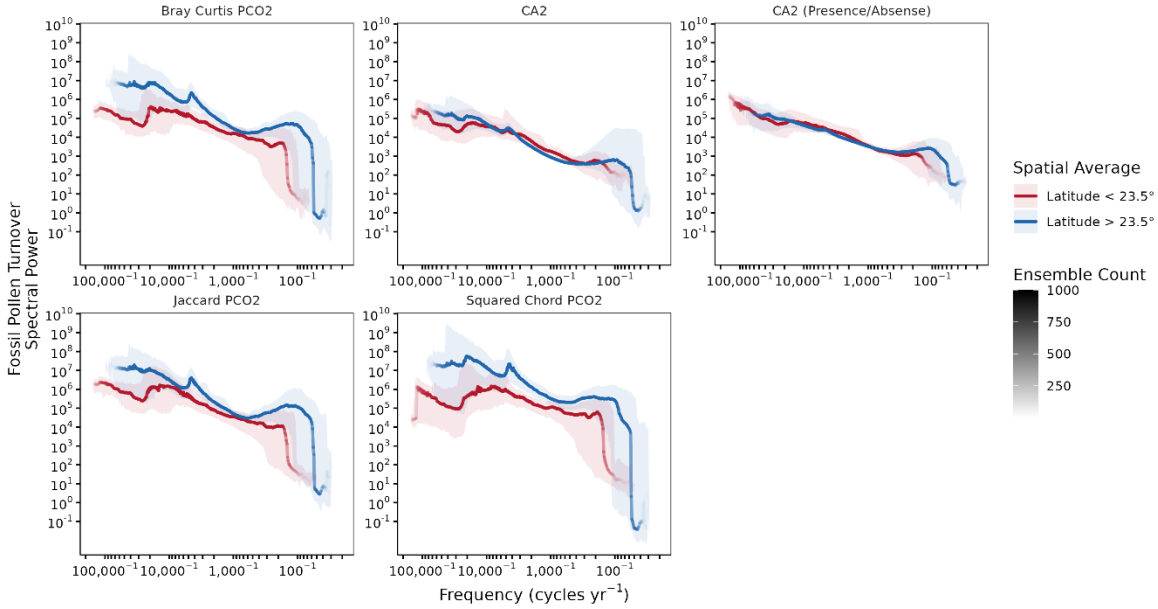

Figure S12. As in Figure S11 but for PCO2 from fossil pollen assemblages.

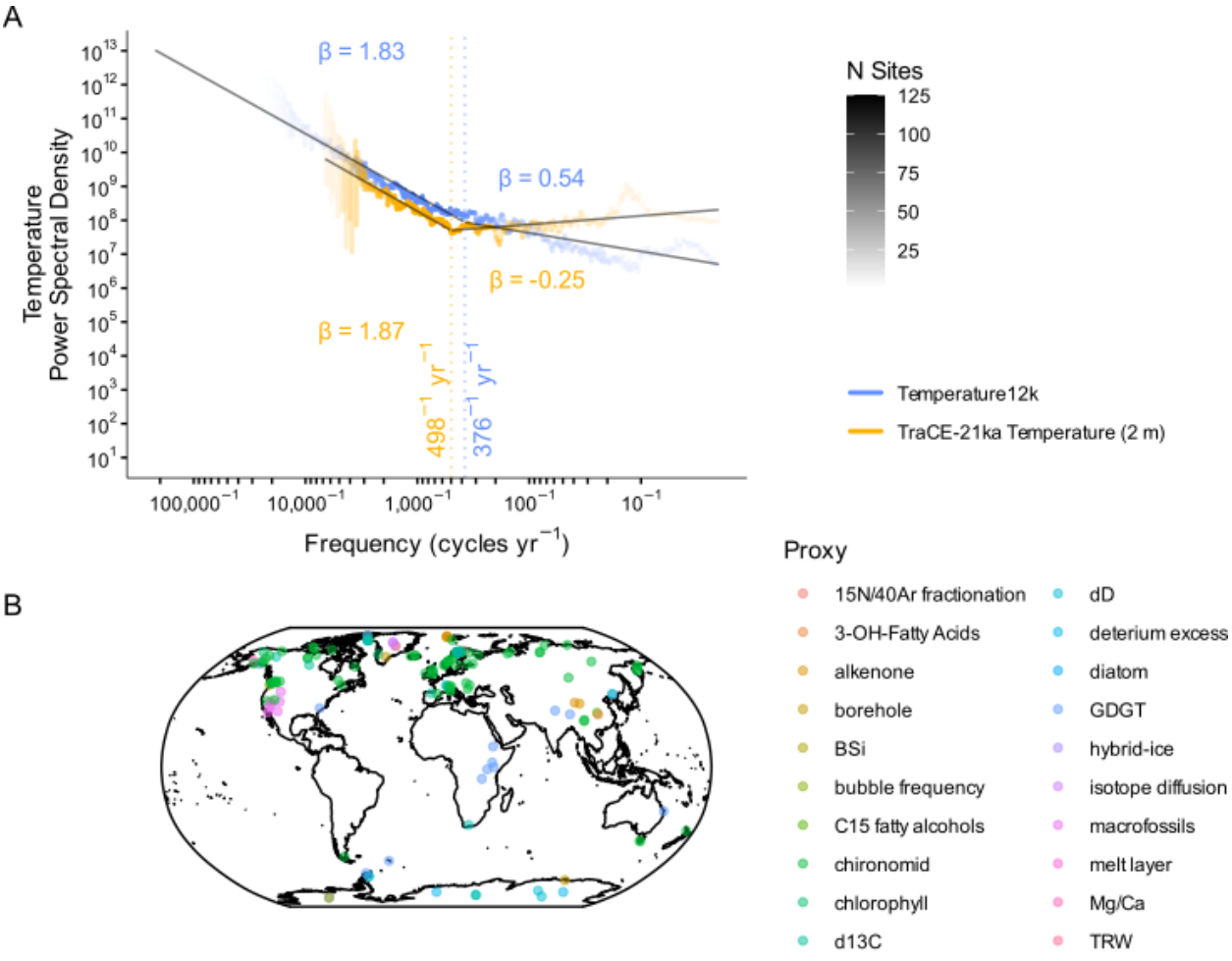

Figure S13. A) The averaged power spectrum for non-pollen temperature estimates from Temperature 12k (yellow). The averaged power spectrum of temperature variability for TraCE-21ka (blue) is estimated after degrading TraCE-21ka to match the time-averaged and spatial characteristics of the Temperature12k sites. Power spectra line opacity indicates the number of sites that resolve each frequency. Note, the similar β at low frequencies and the similar break location between the high frequency and low frequency scaling regimes. B) The Temperature12k sites are colored by proxy.

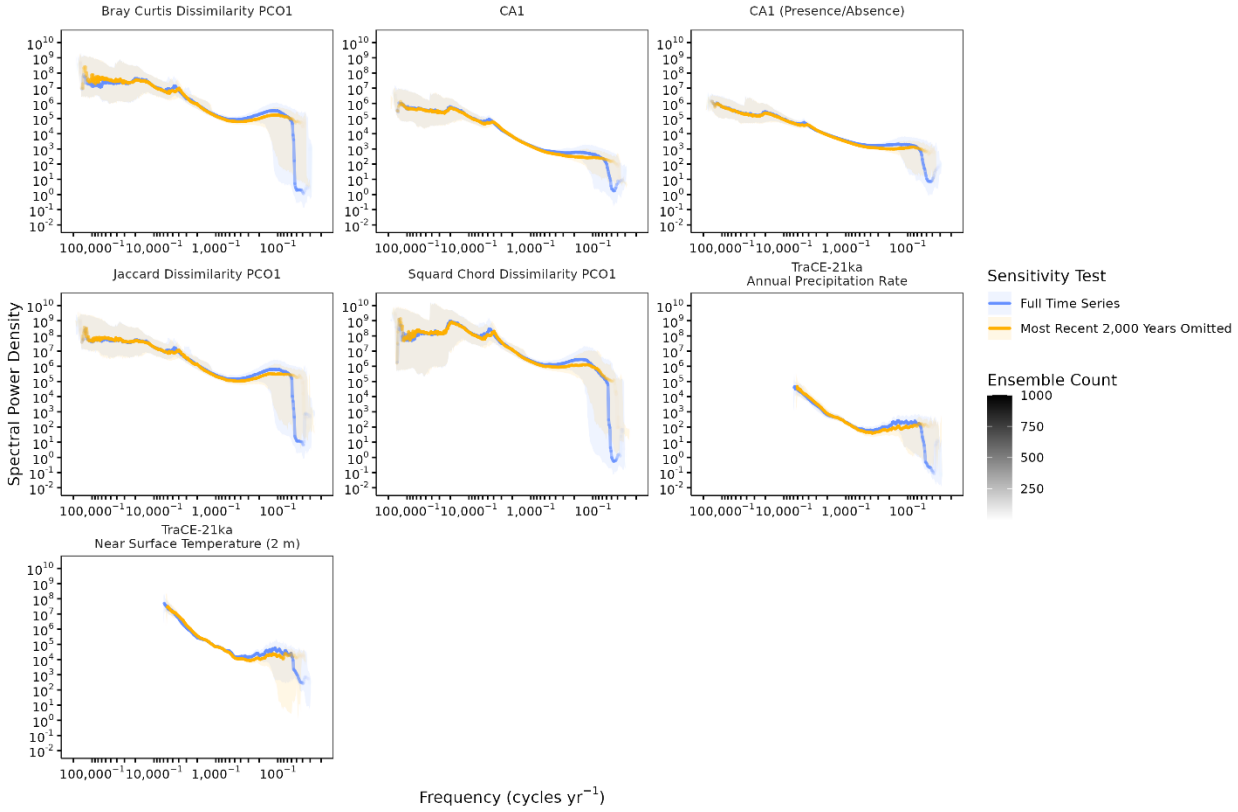

Figure S14. Sensitivity tests for the continuum of vegetation turnover and climate variability based on the median of an ensemble of spectral power estimates after removing any observations younger than 2,000 years to assess the influence of anthropogenic land use change. The blue line corresponds to results from Figure 2 and Figure S3 and the yellow line corresponds to the sensitivity test. Power spectra line opacity indicates the number of ensemble members that resolve each frequency. Note, that the confidence intervals for the power spectra overlap across all of frequency space suggesting a limited influence of anthropogenic land use change.

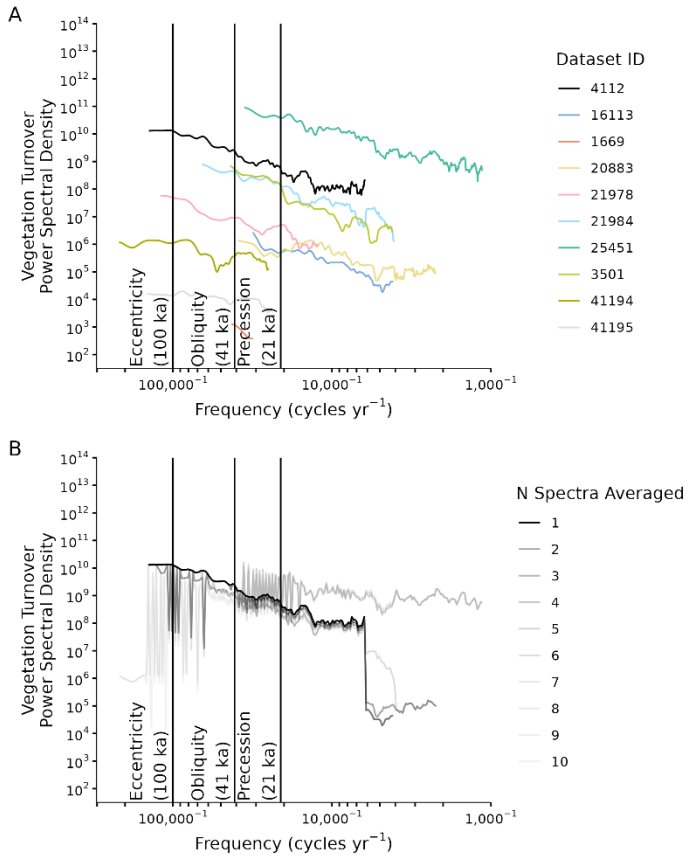

Figure S15. A) Spectral power from the ten longest records from our Neotoma compilation. High spectral power at all Milankovitch bands is particularly well expressed at ODP Site 658 (41194) and Páramo de Agua Blanca (21978). B) The effect of averaging spectral power across these sites, each with a unique sampling resolution and temporal span. Here, the averaging is a running mean from the site order in A. For instance, "N Spectra Averaged" of one is the Ioannina (4112) record; a value of two is the average of Ioannina (4112) and Grays Lake (16113); a value of three is the average of Ioannina (4112), Grays Lake (16113), and Lake Louise (1669). We use the median Bchron age model in these analyses and do not employ the resampling procedure of the main manuscript.

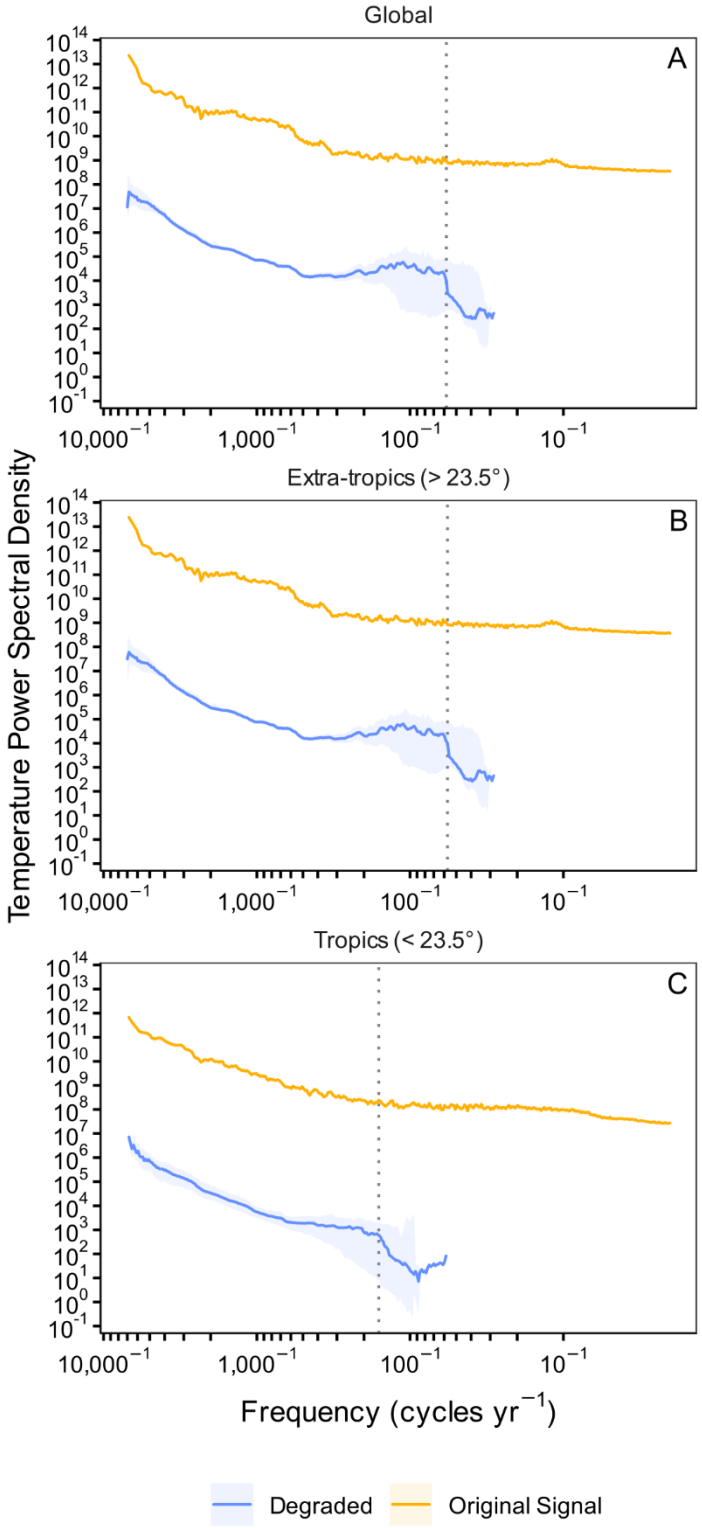

Figure S16. Spectral power for near-surface temperature for TraCE-21ka at each fossil pollen site where the temperature time series is resolved annually (yellow) and degraded (blue) to match the temporal characteristics of the fossil pollen assemblage. For degradation, each annually-

resolved temperature time series corresponding to the nearest grid cell to the fossil pollen site being analyzed was temporally subsampled to match the fossil pollen abundances and then smoothed using a low-pass filter with a timescale twice the mean resolution of the fossil pollen abundances (*58*). The frequency associated with a spurious drop in spectral power in the degraded power spectra, not present in the annually resolved power spectra, is defined as the highest resolvable frequency for (A) global, (B) extra-tropical, and (C) tropical spectral power estimates and marked with a dashed line. These frequencies are 58^{-1} $years^{-1}$, 57^{-1} $years^{-1}$, and 160^{-1} $years^{-1}$, respectively. Confidence intervals result from a Monte-Carlo resampling procedure outlined in *Uncertainty Estimation*.